UNIVERSITY
OF TRENTO

DEPARTMENT OF INFORMATION AND COMMUNICATION TECHNOLOGY

38050 Povo – Trento (Italy), Via Sommarive 14
http://www.dit.unitn.it

A COMPUTATIONAL APPROACH BASED ON A PARTICLE SWARM OPTIMIZER FOR MICROWAVE IMAGING OF TWO-DIMENSIONAL DIELECTRIC SCATTERERS

Massimo Donelli, , and Andrea Massa

August 2004

Technical Report DIT-04-076

A Computational Approach based on a Particle Swarm Optimizer for Microwave Imaging of Two-Dimensional Dielectric Scatterers

Massimo Donelli, *Member, IEEE*, and Andrea Massa, *Member, IEEE*

Department of Information and Communication Technologies,

University of Trento, Via Sommarive 14, I-38050 Trento - Italy

Tel. +39 0461 882057, Fax +39 0461 882093

E-mail: *andrea.massa@ing.unitn.it*, *massimo.donelli@dit.unitn.it*

Web-page: *http://www.eledia.ing.unitn.it*

A Computational Approach based on a Particle Swarm Optimizer for Microwave Imaging of Two-Dimensional Dielectric Scatterers

Massimo Donelli and Andrea Massa

Abstract

A computational approach based on an innovative stochastic algorithm, namely the Particle Swarm Optimizer (PSO), is proposed for the solution of the inverse scattering problem arising in microwave imaging applications. The original inverse scattering problem is reformulated in a global nonlinear optimization one by defining a suitable cost function, which is minimized through a customized PSO. In such a framework, the paper is aimed at assessing the effectiveness of the proposed approach in locating, shaping, and reconstructing the dielectric parameters of unknown two-dimensional scatterers. Such an analysis is carried out by comparing the performance of the PSO-based approach with others state-of-the-art methods (deterministic as well as stochastic) in terms of retrieval accuracy as well as from a computational point of view. Moreover, an integrated strategy (based on the combination of the PSO and the iterative multi-scaling method (IMM)) is proposed and analyzed to fully exploit complementary advantages of nonlinear optimization techniques and multi-resolution approaches. Selected numerical experiments, concerning dielectric scatterers different in shape, dimension, and dielectric profile, are performed starting from synthetic as well as experimental inverse scattering data.

Key words:

Microwave Imaging, Inverse Scattering, Particle Swarm Optimizer.

1 Introduction

In the last years, microwave-imaging techniques have gained a considerable attention from the research community since they can be suitably used for a number of important engineering applications ranging from medical diagnostics [1][2] to non-destructive evaluation [3][4] and subsurface detection [5]. Certainly, one of the most challenging tasks in defining a microwave imaging method is to implement a reliable numerical procedure for the inversion of scattered data. Towards this end, many effective computational techniques have been proposed based on deterministic as well as stochastic optimizers since now-a-day, the leading way to face an inverse scattering problem is to recast it into an optimization one, which is successively solved by means of a minimization technique. In such a framework, let us consider the approaches proposed in [6], [7], [8], and [9]. Unfortunately, the use of iterative procedures often makes the reconstruction process computationally expensive.
From a computational point of view, deterministic techniques (e.g., conjugate gradient methods [10], [11]) are very attractive. However, when local-type inversion procedures are used, accurate and reliable results can be obtained only if the starting trial solution is close enough to the "actual" solution. In many practical cases, such a starting point is not available and some inaccuracies or artifacts in the reconstruction occur because of the presence of false solutions corresponding to local minima of the cost function.
The use of Genetic Algorithms (GAs) [12], [13], [14] would in principle avoid such a circumstance. However, various numerical parameters must be carefully calibrated and customized to the application in hand. Moreover, several options of implementation within evolution operators should be evaluated to select the best operator for a given application. In order to overcome or limit such drawbacks, Kennedy and Eberhart proposed in 1995 [15] the PSO, which is a robust stochastic search procedure inspired to the social behavior of insects swarms. In fact, the main advantages of the PSO over the GA are:

- The *algorithmic simplicity* - The GA considers three genetic operators and one has to choose the best configuration among several options of implementation. On the

contrary, the PSO considers one simple operator, that is the *velocity updating*;

- The *easy manipulation of the calibration parameters* - As far as the GAs are concerned, the calibration parameters to be set are: the population size I, the crossover rate P_c, the mutation rate P_m, and the allele-mutation rate P_{bm} according to the operators implementation. The PSO requires the selection of the dimension of the swarm I, the inertial weight w, as well as the acceleration coefficients C_1 and C_2. Then, if the number of control parameters is the same, certainly it is easier to manipulate the PSO's parameters than evaluating the optimal values among various operators.

- The *ability to prevent the stagnation* - In GAs, the stagnation occurs when the individuals assume a genetic code close to that of the fittest chromosome of the overall population. In such a situation, the crossover operator has little effect and only a lucky mutation could locate a new individual in another attraction basin. On the contrary, in the PSO, a suitable control of the inertial weight and of the acceleration coefficients allows to find new fittest locations in the solution space.

Taking into account these features, PSO has been employed with success in several problems in the framework of applied and computational electromagnetics where GAs found great success (let's see [16], [17], and [18] for some applications in the field of antenna synthesis and [19] for a general overview). Therefore, it turns out profitable to evaluate the effectiveness of the PSO in dealing with microwave imaging problems where GAs have found a great success and widespread implementation. Towards this end, the present paper proposes an innovative computational approach based on a customized PSO for the numerical solution of the inverse scattering problem.

The paper is structured as follows. A brief description of a standard two-dimensional microwave imaging problem will be given in Sect. 2 where a suitable cost function will be defined in order to reformulate the original nonlinear inversion problem in an optimization one. Then a detailed explanation of the PSO algorithm and of its customization to the

microwave imaging framework will be presented in Sect. 3. Sect. 4 will be devoted to the calibration of the PSO's parameters. The parameters selection strategy will be presented and the results of an exhaustive analysis will be discussed to point out the degree of dependence of the minimization process on the parameters values. In Sect. 5, a comparative numerical assessment will be performed by considering different scattering scenarios and various environmental conditions. Moreover, the improvements achievable from an integration of the PSO-based approach with the IMM will be detailed. Finally some conclusions will be drawn and future developments will be proposed (Sect. 6).

2 Microwave Imaging Problem - Mathematical Formulation

Let us consider an inaccessible investigation domain D_I containing a cylindrical scatterer of arbitrary bounded cross-section and modeled by the following object function

$$\tau(x,y) = [\varepsilon_r(x,y) - 1] - j\frac{\sigma(x,y)}{2\pi f} \quad (x,y) \in D_{object} \subset D_I \tag{1}$$

$\varepsilon_r(x,y)$ and $\sigma(x,y)$ being the relative dielectric permittivity and the electric conductivity, respectively; f is the working frequency. Such an investigation region is successively illuminated by a set of V incident transverse-magnetic waves characterized by z-directed electric fields $\mathbf{E}^v_{inc}(\mathbf{r}) = E^v_{inc}(x,y)\widehat{z}$, $v = 1, \ldots, V$. The scattered fields $\mathbf{E}^v_{scatt}(\mathbf{r}) = E^v_{scatt}(x,y)\widehat{z}$, $(x,y) \notin D_I$ arising from multiple-scattering interactions between incident waves and the unknown object are collected in $m_{(v)} = 1, ..., M_{(v)}$, $v = 1, ..., V$, measurement points located in an area, called observation domain D_O, external to the investigation domain D_I. The background medium is assumed to be homogeneous, non-magnetic, and lossless with dielectric permittivity ε_0.

The imaging process is aimed at retrieving the distribution of the object function (1) and of the electric field $E^v_{tot}(x,y)$ $(x,y) \in D_I$ starting from the knowledge of the scattering

data ($E^v_{scatt}(x_{m_{(v)}},\, y_{m_{(v)}})$, $m_{(v)} = 1, ..., M_{(v)}$, $v = 1, ..., V$ and $E^v_{inc}(x, y)$, $(x, y) \in D_I$), by modeling the nonlinear electromagnetic interactions through the well-known Lippmann-Schwinger integral equations [20]

$$E^v_{scatt}(x_{m_{(v)}},\, y_{m_{(v)}}) = k_0^2 \int_{D_I} G_0(x_{m_{(v)}},\, y_{m_{(v)}};\, x', y') E^v_{tot}(x', y') \tau(x', y')\, dx' dy' \qquad (x_{m_{(v)}},\, y_{m_{(v)}}) \in D_O \tag{2}$$

$$E^v_{inc}(x, y) = E^v_{tot}(x, y) - k_0^2 \int_{D_I} G_0(x, y;\, x', y') E^v_{tot}(x', y') \tau(x', y')\, dx' dy' \qquad (x, y) \in D_I \tag{3}$$

where G_0 is the two-dimensional free-space Green function given by $G_0(x, y; x', y') = \frac{j}{4} H_0^{(2)}\left(k_0 \sqrt{(x - x')^2 + (y - y')^2}\right)$, $H_0^{(2)}$ being the Hankel function of 0-*th* order and second kind.

To numerically deal with Eqs. (2) and (3), the Richmond's method [21] is applied and the discretized counterparts of the inverse scattering integral equations are obtained. Consequently, the problem unknowns are represented through a linear combination of rectangular basis functions ($R_n(x, y)$, $n = 1, ..., N$) as follows

$$\tau(x, y) = \sum_{n=1}^{N} \tau_n R_n\,(x, y) \qquad (x, y) \in D \tag{4}$$

$$E^v_{tot}(x, y) = \sum_{n=1}^{N} \psi_n^{(v)} R_n\,(x, y) \qquad (x, y) \in D \tag{5}$$

Then, the inverse problem is recast into the global minimization of the cost function ϕ

$$\phi(\underline{f}) = \frac{\sum_{v=1}^{V} \sum_{m_{(v)}=1}^{M_{(v)}} \left| E^v_{scatt}(x_{m_{(v)}}, y_{m_{(v)}}) - \Im^{v,m}_{Data}\left\{\tau_n, \psi_n^{(v)}\right\} \right|^2}{\sum_{v=1}^{V} \sum_{m_{(v)}=1}^{M_{(v)}} \left| E^v_{scatt}(x_{m_{(v)}}, y_{m_{(v)}}) \right|^2} + \frac{\sum_{v=1}^{V} \sum_{n=1}^{N} \left| E^v_{inc}(x_q, y_q) - \Im^{v,n}_{State}\left\{\tau_n, \psi_n^{(v)}\right\} \right|^2}{\sum_{v=1}^{V} \sum_{n=1}^{N} \left| E^v_{inc}(x_q, y_q) \right|^2} \tag{6}$$

where $\underline{f} = \left\{\tau_n,\, \psi_n^{(v)};\, n = 1, ..., N;\, v = 1, ..., V\right\} = \{f_j;\, j = 1, ..., J;\, J = N \times V\}$; $\Im_{Data}$ and $\Im_{State}$ being the discretized form of the right-hand-side terms of equations (2) and (3), respectively.

Finally, the solution of (6) is obtained by constructing a sequence $\left\{\underline{f}^{(k)};\, k = 1, ..., K\right\}$, k

being the iteration number, which converges to $\underline{f}^{opt} = arg\left\{min_{\underline{f}}\left[\phi(\underline{f})\right]\right\}$. Towards this end, a suitable PSO-based technique is adopted.

3 Application of the Particle swarm algorithm

PSO is a *multiple-agent* optimization procedure in which individuals, called *particles*, change their positions (or *state*) with time. In a PSO system, particles fly around in the multidimensional solution space and adjust their positions according own experience and the experience of neighboring particles, by exploiting the knowledge of best positions encountered by their-self and their neighbors.

In order to describe the particle swarm algorithm, let us consider a *swarm* of I individuals $\Omega = \{\varsigma_i;\ i = 1,\ ...,\ I\}$ (I being the dimension of the set of trial solutions) where each particle ς_i is characterized by a position $\underline{f}_i$ in the solution space (i.e., the ith trial solution of the microwave imaging problem)

$$\underline{f}_i = \{f_{i,j};\ j = 1,\ ...,\ J\} \tag{7}$$

and a velocity $\underline{s}_i$

$$\underline{s}_i = \{s_{i,j};\ j = 1,\ ...,\ J\} \tag{8}$$

, which models the capability of the ith particle to fly from the current position $\underline{f}_i^{(k)}$ (i.e., its position at the kth iteration of the minimization process) to another successive position $\underline{f}_i^{(k+1)}$ in the solution space.

Then, the developed iterative procedure consists of the following steps.

- *Step* 0 - ***Initialization***. Initialize the iteration counter $k = 0$. Randomly generate a swarm of I particles $\Omega^{(k)} = \left\{\varsigma_i^{(k)};\ i = 1,\ ...,\ I\right\}$ and associated positions $\underline{f}_i^{(k)}$ and velocities $\underline{s}_i^{(k)}$, $i = 1,\ ...,\ I$. $f_{i,j}^{(k)}$ is set by randomly selecting a value with uniform probability over the search space of the jth parameter ($f_{i,j}^{(k)} \in \left[\xi_j^{min},\ \xi_j^{max}\right]$) defined according to the available *a-priori* information. Similarly, a random value in the

range $[-S_j, S_j]$, S_j being a threshold value, is assigned to $s_{i,j}^{(k)}$. Set the value of the inertial weight $w^{(k)}$.

- *Step* 1 - ***Fitness Evaluation***. Rank each particle according to its fitness value computed trough the cost function (6), $\phi_i^{(k)} = \phi\left\{\underline{f}_i^{(k)}\right\}$, $i = 1, ..., I$. For each particle, compare the fitness value of $\varsigma_i^{(k)}$ to the best fitness that the particle has ever attained at any iteration up to current one, $\phi\left\{\underline{p}_i^{(k-1)}\right\} = min_{h=1,...,k-1}\left(\phi\left\{\underline{f}_i^{(h)}\right\}\right)$ and update the "*pbest*" trial solution $\underline{p}_i^{(k)} = \underline{f}_i^{(k)}$ if $\phi\left\{\underline{f}_i^{(k)}\right\} < \phi\left\{\underline{p}_i^{(k-1)}\right\}$. Search for the optimal particle of the current iteration, $\varsigma_{opt}^{(k)}$, which position is defined as $\underline{f}_{opt}^{(k)} = arg\left[min_i\left(\phi\left\{\underline{f}_i^{(k)}\right\}\right)\right]$ and update the "*gbest*" particle of the swarm $\underline{g}^{(k)} = \underline{f}_{opt}^{(k)}$ if $\phi\left\{\underline{f}_{opt}^{(k)}\right\} < \phi\left\{\underline{g}^{(k-1)}\right\}$.

- *Step* 2 - ***Iteration Updating***. Update the iteration index $k \leftarrow k + 1$.

- *Step* 3 - ***Convergence Check***. If the *termination criterion*, based on a maximum number of iterations K (i.e., $k > K$) or on a threshold for the fitness value (i.e., $\phi\left\{\underline{g}^{(k)}\right\} \leq \eta$), is satisfied then set $\underline{f}^{opt} = \underline{g}^{(k)}$ and stop the minimization process. Otherwise, go to Step 4.

- *Step* 4 - ***Velocity Updating***. By using the knowledge of the global best and of the individual best particles, $\underline{g}^{(k)}$ and $\underline{p}_i^{(k)}$, $s_{i,j}^{(k)}$ is updated according to the following equation [22]:

$$s_{i,j}^{(k+1)} = w s_{i,j}^{(k)} + C_1 r_1\left\{p_{i,j}^{(k)} - f_{i,j}^{(k)}\right\} + C_2 r_2\left\{g_j^{(k)} - f_{i,j}^{(k)}\right\} \tag{9}$$

  where r_1 and r_2 are uniform random numbers between 0 and 1; C_1 and C_2 are two positive constants called *acceleration coefficients*. They represent the weight of the "cognition" and "social" part that pulls ς_i from $\underline{f}_i^{(k)}$ towards the "*pbest*" $\underline{p}_i^{(k)}$ and the "*gbest*" $\underline{g}^{(k)}$ positions [23], respectively.

- Step 5 - ***Boundary Conditions Check***. To reduce excessively large step sizes in

the particle's fly, clamp $\left|s_{i,j}^{(k)}\right|$ to a specified maximum value S_j (according to the reference literature [24], [25], [19], S_j is set to the dynamic range of the jth dimension). Moreover, to limit the search space of the swarm to the physically admissible solution space, change the sign of $s_{i,j}^{(k)}$ ("*reflecting wall*" boundary condition [19]) when $f_{i,j}^{(k)}$ turns out to be out of the physical range.

- Step 6 - ***Position Updating***. According to the updated velocity value (Step 4 and Step 5), change the position of $\varsigma_i^{(k)}$ as follows

$$f_{i,j}^{(k+1)} = f_{i,j}^{(k)} + s_{i,j}^{(k+1)} \tag{10}$$

then go to Step 1.

A flowchart of the algorithm is shown in Fig. 2.

4 Numerical Analysis

The aim of this section is twofold. Firstly, the results of an extensive analysis of the impact of the PSO parameters on the approach performance are reported to determine the ideal configuration for microwave imaging problems. Then, by considering the so-defined optimal setting, the effectiveness and robustness of the PSO-based approach are assessed in reconstructing different scattering scenarios starting from synthetically-generated as well experimental inverse scattering data.

4.1 Sensitivity Analysis

In the interests of presenting a reliable general purpose PSO-based approach for microwave imaging, a sensitivity study has been performed. Towards this end, three experiments have been carried out:

- *Experiment 1* - The swarm size I has been varied to determine its role in achieving the global optimum of the cost function (6);

- *Experiment 2* - The value of the inertial weight w has been varied according to the suggestions in the reference literature to achieve a good balance between global and local exploration during the minimization;

- *Experiment 3* - The values of the acceleration coefficients, $C_1$and C_2, have been varied in the range of admissible values.

As reference scenario, the following geometry has been considered. A square investigation domain, $L_{DI} = \lambda_0$ in side, illuminated by a set of $V = 4$ TM-polarized plane waves and partitioned in $N = 15 \times 15$ equal square sub-domains ($U = 2250$ being the number of problem unknowns). A circular observation domain $R_O = 0.9\,\lambda_0$ in radius where $M_{(v)} = 21$ measurement points equally-spaced are located. In such a scenario, various scatterers, different in shape and dimensions, have been probed. A circular cylinder, centered at $x_c = y_c = 0.3\,\lambda_0$, of diameter $d = 0.8\lambda_0$ and characterized by a homogeneous object function value $\tau(x, y) = 0.5$ (Test Case 1) and $\tau(x, y) = 2.0$ (Test Case 2), respectively. A square ($L = 0.4\,\lambda_0$-sided) cylinder characterized by a homogeneous object function value $\tau(x, y) = 0.5$ and centered at $x_c = y_c = 0.0\,\lambda_0$ (Test Case 3) and $x_c = y_c = 0.4\,\lambda_0$ (Test Case 4), respectively.

In the numerical experiments, to take into account the stochastic nature of the algorithm, each test case has been repeated $L = 100$ times with the same PSO-parameters combination and the average optimal function value Φ defined as

$$\Phi = av_{l=1,\ldots,L}\left[\phi\left\{\underline{f}^{opt}\right\}\right] \tag{11}$$

has been recorder. The obtained results will be summarized in graphical form and discussed in the following sub-sections.

4.1.1 Swarm dimension, I

As a general rule for population-based methods, it is evident that a small dimension will produce a notable reduction of the computational burden, but the possibility that the solution be trapped in a local minimum could increase. On the contrary, large populations will tend to lessen the required swarm iterations at the cost of more fitness evaluations and computation time.

As far as the PSO is concerned, the effect of the swarm size has been extensively studied (see [26] [27] for a detailed description) and it is quite common in PSO-research to limit the number of particles to the range between $I = 20$ and $I = 60$ [24], which seems a reasonable compromise between cost and reliability. van den Berg and Engelbrecht [28] suggested that even though there is a slight improvement of the optimal value by enlarging the swarm size, it increases the number of function evaluations to reach the convergence threshold.

However, it should be pointed out that above indications have been generally drawn for low-dimension solution spaces. Consequently, concerning a high-dimensional space as for microwave imaging, I needs a careful analysis to assess if suggested numerical values are again suitable. Then an experiment has been carried out by ranging the swarm dimension from $I = 1$ (corresponding to a percentage of 0.04 % of the total amount of problem unknowns U) up to $I = 800$ (equal to a percentage of 35 % of U). Other PSO-parameters have been set following common practice in the literature: $C_1 = C_2 = 2.0$ [25] and a constant inertial weight equal to $w = 0.4$ [29]. Since it is not the objective of this analysis to test the performance of different stopping criteria, but rather the PSO algorithm itself, a simple *a-priori* stopping criterion is used. The minimization has been terminated at the maximum number of iterations ($K = 10000$).

Figure 4 shows the plot of the average optimal function value Φ versus the swarm size I for each test case. As can be observed, a threshold of $-40\,dB$ is already reached for swarm dimensions of about $I \simeq 30 \div 55$ particles ($\zeta_I \simeq 1.33 \div 2.44$, being $\zeta_I = \frac{I}{U} \times 100$).

For larger populations ($I \geq 400 \Rightarrow \zeta_I \simeq 17$), the value of Φ further decreases and it turns out to be equal to $-50\,dB$. Then, as a general rule, a number of particles between $I = 45$ ($\zeta_I = 3$) and $I = 200$ ($\zeta_I = 15$) seems to be a suitable choice to allow a good balance among minimization properties and amount of required computer time.

4.1.2 Inertial weight

The right-hand side of (9) consists of three terms. The first term (sometimes referred as *inertia*), introduced in [29] by Shi and Eberhart, is proportional to the old velocity of the particle $s_{i,j}^{(k)}$ through a scalar component w. Higher values for w produce relatively straight particle trajectories resulting in a good global search characteristic. Small values for w encourage a local searching. Consequently, some researchers find advantage that w decreases during the minimization process to allow a refined local search at the end of the optimization [26][27] or randomly varies during the iterative procedure [30]. For this study, w is taken to be a constant throughout the iterative process.

Certainly, a key issue in the introduction of a constant inertia is the definition of its optimal value. Towards this end, w has been ranged between 0.0 and 1.4. Concerning the PSO-parameters configuration, the following values have been chosen: $C_1 = C_2 = 2.0$, $K = 10000$, and $I = 20$.

Figure 4 shows the behavior of Φ versus the inertial weight w. As can be observed, the plot of the average optimal cost function value presents a minimum when $w \simeq 0.4$, which will be assumed in the following as the optimal value.

4.1.3 Acceleration Terms

The second and third term of (9) are used to avoid that the particle ς_i keeps on "flying" the same direction until it hints the boundary of the search space. They correspond to an intensification in the search procedure. C_1 is referred as *memory* and it regulates the attraction of the particle towards its personal best position $\underline{p}_i^{(k)}$. The term called *cooperation* C_2 weights the stochastic acceleration that pulls ς_i towards $\underline{g}^{(k)}$.

Usually, C_1 and C_2 are set to 2.0 as recommended by PSO literature [15][22][29] and found through experimentation in several optimization fields [18]. To assess the effectiveness of such a setting also in the microwave imaging framework, a sensitivity study has been carried out by varying the values of C_1 and C_2 from 0.0 up to 5.0 (by assuming that $I = 20$, $K = 10000$, and $w = 0.4$).

As an example, Fig. 5 shows a pictorial representation of Φ versus the acceleration parameters C_1 and C_2 for the Test Case 1 (similar behaviors have been obtained for the other test cases, as well). The two-dimensional surface presents two minima corresponding to the following parametric configurations: $C_1 = C_2 = 2.0$ and $C_1 = 0.3$ and $C_2 = 2.5$. According to these observations and following common practice in the literature, the acceleration parameters have been set to $C_1 = C_2 = 2.0$.

In conclusion, after the calibration phase, the following values seems to be appropriate for a microwave imaging problem: $\zeta_I = 5.5$, $w = 0.4$, and $C_1 = C_2 = 2.0$. If it is not specified, such a configuration will be used in the numerical assessment.

4.2 Numerical Assessment

In this section, the potentialities of the proposed PSO-based microwave imaging method will be assessed by presenting a selected set of results from several numerical experiments. The behavior of the proposed method will be illustrated by considering three different classes of scatterers: reference objects for which analytical scattering solutions are available (Sect. 4.2.1), homogeneous scatterers (Sect. 4.2.2), and inhomogeneous scatterers (Sect. 4.2.3 and Sect. 4.2.4) in noiseless as well as noisy conditions. Moreover, the numerical validation will consider experimentally-acquired data (Sect. 4.3) for an check in a real framework.

The obtained results will be compared with those of state-of-the art numerical procedures (namely, the CG-based approach and the GA-based method). Moreover, the improvement allowed by the PSO when integrated with the IMM [31] will be shown.

During the numerical validation, the following parameters and error figures will be used

- *Signal-to-Noise Ratio* (SNR):

$$SNR = 10log_{10}\frac{\sum_{v=1}^{V}\sum_{m_{(v)}=1}^{M_{(v)}}\left|E^{v}_{scatt}(x_{m_{(v)}},\, y_{m_{(v)}})\right|^2}{2MV\sigma^2_{noise}} \tag{12}$$

  where σ^2_{noise} is the variance of the additive Gaussian noise (with zero mean value);

- *Reconstruction Errors* (ε_{tot}, ε_{int}, and ε_{ext})

$$\varepsilon_{(u)} = \frac{1}{N_{(u)}}\sum_{n_{(u)}=1}^{N_{(u)}}\left\{\frac{\widetilde{\tau}(x_{n_{(u)}},\, y_{n_{(u)}}) - \tau(x_{n_{(u)}},\, y_{n_{(u)}})}{\tau(x_{n_{(u)}},\, y_{n_{(u)}})}\right\} \times 100 \tag{13}$$

  where $N_{(u)}$ can range over the whole investigation domain ($u \Rightarrow tot$), or over the area where the actual scatterer is located ($u \Rightarrow int$), or over the background belonging to the investigation domain ($u \Rightarrow ext$); the super-script $\widetilde{}$ is related to the reconstructed values;

- *Qualitative Imaging Errors* (ρ and δ)

$$\rho = \frac{\sqrt{[\widetilde{x}_c - x_c]^2 + [\widetilde{y}_c - y_c]^2}}{\lambda_0} \qquad (Localization\ Error) \tag{14}$$

$$\delta = \left\{\frac{\widetilde{L} - L}{L}\right\} \times 100 \qquad (RoI\ Estimation\ Error) \tag{15}$$

4.2.1 Off Centered Circular Cylinder

The first test case deals with a homogeneous ($\tau(x, y) = 2.0$) circular cylinder of diameter $d = 0.3\,\lambda_0$ and centered at $x_c = y_c = 0.15\,\lambda_0$. Since the simple object, for which a closed solution of the scattered field can be found [32], the values of the scattering data $E^{v}_{scatt}(x_{m_{(v)}},\, y_{m_{(v)}})$ have been analytically computed.

Such an example is firstly aimed at comparing the capabilities of the proposed PSO-based approach to those of similar iterative procedures based on CG [33] and GA [34].

For comparison purposes, the same population of $I = 100$ individuals has been considered for the PSO as well as for the GA-based approach. Moreover, concerning the other GA parameters, the following configuration (as suggested in the literature [35]) has been used: $P_c = 0.8$ (*crossover* probability) and $P_m = 0.04$ (*mutation* probability).

Figure 6 shows grey-level images[1] of the reconstructed object functions. In particular, Figs. 6(a)-(c) give the reconstructed images obtained by applying the PSO-approach, the CG-based method, and the GA-based approach. The ideal reconstruction (with respect to the adopted discretization, $N = 15 \times 15$) is also reported (Fig. 6(d)). As can be noted, the unknown scatterer is correctly localized whatever method is used ($\rho < 10^{-2}$). However, a more accurate representation of the actual profile is reached with the PSO-based approach as confirmed and supported by the values of the error figures given in Tab. I. More in detail, it turns out that the PSO-based approach considerably outperforms the CG-based approach in cleaning the external background ($\varepsilon_{ext}^{(PSO)} = 1.52$ vs. $\varepsilon_{ext}^{(CG)} = 9.71$) and reconstructing the actual dielectric profile ($\varepsilon_{int}^{(PSO)} = 3.91$ vs. $\varepsilon_{int}^{(CG)} = 18.39$). Moreover, it better estimates the object shape than the GA-based method by obtaining an error in defining the *region-of-interest* (RoI)[2] equal to $\delta^{(PSO)} = 5.38$ (vs. $\delta^{(CG)} = 9.91$).

For completeness, Fig. 7 shows the behavior of the optimal value of the cost function $\phi^{(k)} = \phi\left\{\underline{g}^{(k)}\right\}$ during the iterative process for each of the optimization approaches.

The second experiment is devoted to evaluate the robustness of the PSO-based approach to the noise. Towards this aim, an additive Gaussian noise has been added to the scattering data by considering different SNRs in the range between $20\,dB$ and $5\,dB$. As expected, the presence of the noise causes a deterioration of the reconstruction and localization accuracy as indicated by the errors figures pictorially represented in Fig. 8. However, this example demonstrates that even under noisy circumstances, the PSO-based approach is able to reach a satisfactory retrieval in terms of qualitative as well as quantitative imaging (except for the situation characterized by a $SNR = 5\,dB$ for which $\rho > 10^{-1}$). In fact, it

[1] Please note that the black pixel in the lower right border is used for reference and the dashed line indicates the region occupied by the actual scatterer.

[2] The RoI is defined as that minimal square region to which the scatterer belongs.

should be noted that the values of the quantitative error figures do not exceed 11 % (a value of the same order in magnitude of the reconstruction error ε_{tot} achieved with the CG-based approach, but for noiseless conditions, $\varepsilon_{tot}^{(CG)} = 10.21$ - Tab. I).

However, as pointed out in [31], to achieve an improvement in the resolution accuracy, even though in presence of a limited amount of information in the scattering data [36], it could be profitable to consider a multi-resolution strategy in place of a "*bare*" (or *single step*) approach. Such a strategy, called Iterative Multi-resolution Method, allows a synthetic zoom of the RoI and it is not dependent on the minimization approach. For simplicity, a conjugate-gradient optimizer, based on the alternating direction implicit method [33], has been used in [37]. Then, it could be interesting to evaluate the feasibility and the effectiveness of an integration of the PSO-approach in the IMM strategy. Towards this end, the third experiment has been carried out by considering again the circular scatterer but with an IMM-PSO reconstruction strategy.

Fig. 9 shows the evolution of the reconstruction during the multi-step process. As a reference, the ideal reconstruction is shown in Fig. 9(a). At the end of the first step ($s = 1$, s being the step index) [Fig. 9(b)], the RoI of the unknown scatterer is accurately located ($\rho^{(IMM-PSO)}\Big|_{s=1} = 1.10 \times 10^{-3}$ - Tab. II) with a degree of accuracy greater than that obtained by the bare PSO-approach at the convergence ($\rho^{(PSO)} = 6.0 \times 10^{-3}$ - Tab. I), but the circular shape is not correctly retrieved. Successively ($s = 2$ - [Fig. 9(c)]), the reconstruction improves and at the convergence ($s = S^{opt} = 3$ - [Fig. 9(d)]) a faithful reconstruction is achieved ($\varepsilon_{tot}^{(IMM-PSO)}\Big|_{s=S^{opt}} = 1.01$ vs. $\varepsilon_{tot}^{(PSO)} = 2.49$, $\varepsilon_{int}^{(IMM-PSO)}\Big|_{s=S^{opt}} = 1.14$ vs. $\varepsilon_{int}^{(PSO)} = 3.91$, and $\varepsilon_{ext}^{(IMM-PSO)}\Big|_{s=S^{opt}} = 0.45$ vs. $\varepsilon_{ext}^{(PSO)} = 3.03$).

4.2.2 Centered Square Cylinder

To further analyze the behavior of the integrated IMM-PSO strategy and to evaluate the improvement guaranteed by such an approach, another scattering scenario has been considered. More in detail, the second example refers to a centered homogeneous ($\tau(x, y) = 0.5$) square ($L = 0.8\,\lambda_0$) cylinder located in a larger investigation domain

$L_{DI} = 2.4\,\lambda_0$ in side. Inversion data have been numerically-computed by using the well known Richmond's procedure [21] and, to prevent the so-called "*inverse crime*" problem, a proper discretization of the investigation domain (different from the one which has been employed at each step of the IMM) has been chosen. Concerning the PSO, a swarm dimension of $I = 20$ particles has been set since the problems unknowns turned out to be $U = 360$ ($N^{(IMM-PSO)}\Big|_{s=1} = 6 \times 6$). Moreover, the maximum number of iterations for each scaling step has been fixed to $K = 2000$.

Figure 10 shows the evolution of the reconstruction during the multi-step process. Moreover, the error figures are depicted in Fig. 11. The obtained results show the effectiveness of the IMM-PSO strategy in dealing with such a different geometry, as well. Again, when $s = 1$, the algorithm is able to locate the RoI with a great accuracy ($\rho^{(IMM-PSO)}\Big|_{s=1} = 1.10 \times 10^{-3}$ - Fig. 11). The capability of the algorithm to exactly shape the scatterer significantly improves as the step index increases and, at the final step ($s = S^{opt} = 3$ - [Fig. 10(d)]), the retrieved profile fits very well the actual one in terms of localization ($\rho^{(IMM-PSO)}\Big|_{s=S^{opt}} = 1.20 \times 10^{-5}$), shaping ($\delta^{(IMM-PSO)}\Big|_{s=S^{opt}} = 1.22$) , and quantitative imaging ($\varepsilon_{tot}^{(IMM-PSO)}\Big|_{s=S^{opt}} = 0.49$, $\varepsilon_{int}^{(IMM-PSO)}\Big|_{s=S^{opt}} = 2.21$, and $\varepsilon_{ext}^{(IMM-PSO)}\Big|_{s=S^{opt}} = 5.0 \times 10^{-3}$).

For comparison purposes, Fig. 12 displays the images of the reconstructed profile at $s = S^{opt}$ by considering the IMM-CG strategy [Fig. 12(a)] and the IMM-GA strategy [Fig. 12(b)], respectively. As can be seen, the reconstruction achieved with the IMM-PSO [Fig. 10(d)] outperforms the others (as confirmed by the values of the error figures reported in Tab. III) even though such an improvement turns out to be lower in magnitude with respect to that shown in Tab. I and related to the "bare" approach. However, concerning the minimization process and by observing the behavior of $\phi^{(k)}$ during the iterative process (Fig. 13), it should be noted that the PSO allows a significant decrease of the fitness function of about two order in magnitude. Such a result seems to indicate a better exploitation of the complementary advantages of a nonlinear optimization and a multi-resolution approach when the PSO-based approach is used. Moreover, by comparing

Fig. 7 and Fig. 13, it follows also that the PSO benefits of the multi-resolution strategy (and consequently of a suitable reduction of the solution space) in the minimization of the cost function.

Finally, to assess the stability of the IMM-PSO strategy, an additive gaussian noise has been added to the measured data. Tab. IV shows the achieved results in terms of error figures and for different signal-to-noise-ratio values. Confirming the indications drawn in Tab. I and related to the bare PSO-approach, the PSO-based method turns out to be a reliable technique. More in detail, $\varepsilon_{tot}^{(IMM-PSO)}\Big\rfloor_{s=S^{opt}} < 9.0$ and $\delta^{(IMM-PSO)}\Big\rfloor_{s=S^{opt}} < 7.0$ whatever the SNR value. Moreover, the localization is very accurate ($\rho^{(IMM-PSO)}\Big\rfloor_{s=S^{opt}} < 1.2 \times 10^{-3}$) when ($SNR > 5\,dB$).

4.2.3 Off Centered Hollow Square Cylinder

In the framework of the comparative assessment, a configuration earlier treated in [31] with the IMM integrated with the CG-optimizer has been considered. The unknown scatterer is an off-centered hollow square cylinder located at $x_c = y_c = -0.2\,\lambda_0$ [Fig. 14(a)] of a noisy scenario ($SNR = 30\,dB$). The outer cylinder, $L_{outer} = 1.2\lambda_0$ in side, is characterized by a homogeneous object function $\tau(x, y) = 0.5$. The inner square, characterized by dielectric characteristics equal to that of the background, is $L_{inner} = 0.4\lambda_0$-sided.

As far as the IMM is concerned, the following configuration of the control parameters has been used: $N\rfloor_{s=1} = 6 \times 6$, $K = 2000$, $\eta_x = 1\,\%$, $\eta_y = 1\,\%$, and $\eta_L = 5\,\%$. Moreover, for the PSO, a swarm of $I = 20$ particles has been considered.

The reconstructions at the convergence step (Tab. V) are shown in [Fig. 14(b)] and in [Fig. 14(c)] when the IMM-PSO and the IMM-GC strategy are used, respectively. The advantage of using the IMM-PSO strategy is evident. The accuracy in the resolution of the inner boundary of the scatterer is increased as well as the shaping of the object under test. Consequently, the values of the error figures significantly decreases ($\frac{\varepsilon_{int}^{(IMM-CG)}\Big\rfloor_{s=S^{opt}}}{\varepsilon_{int}^{(IMM-PSO)}\Big\rfloor_{s=S^{opt}}} \simeq 1.80$, $\frac{\varepsilon_{ext}^{(IMM-CG)}\Big\rfloor_{s=S^{opt}}}{\varepsilon_{ext}^{(IMM-PSO)}\Big\rfloor_{s=S^{opt}}} \simeq 2.60$, and $\frac{\delta^{(IMM-CG)}\Big\rfloor_{s=S^{opt}}}{\delta^{(IMM-PSO)}\Big\rfloor_{s=S^{opt}}} \simeq 1.50$)

4.2.4 Centered Multilayer Square Cylinder

In the last test case of the numerical assessment with synthetic scattering data, a more complex configuration has been taken into account as well as noisy conditions ($SNR = 20\,dB$). In such a case, the scattering object consists of centered concentric square cylinders. An inner cylinder of dimension $0.4\,\lambda_0 \times 0.4\,\lambda_0$ with contrast $\tau(x,y) = 2.0$, surrounded by an outer layer, $1.2\,\lambda_0 \times 1.2\,\lambda_0$, characterized by an object function $\tau(x,y) = 0.5$.

For comparison purposes, the results obtained by means of the IMM integrated with the GA will be reported, as well [Fig. 15(b)].

Whatever the method, the shape of the cylinder is recovered with high accuracy and the two layers are clearly distinguishable (Fig. 15). However, the reconstruction effectiveness of the IMM-PSO strategy is highlighted by comparing the horizontal cross-section of the reconstructed profiles [Fig. 15(d)]. As can be observed, the profile retrieved with the IMM-PSO method shows an evident symmetry, which is only partially recovered by the IMM-GA strategy. Such a behavior is also confirmed by the value of the localization error, which reduces ($\rho^{(IMM-PSO)}\Big|_{s=S^{opt}} = 1.8 \times 10^{-3}$ vs. $\rho^{(IMM-GA)}\Big|_{s=S^{opt}} = 3.0 \times 10^{-2}$ - Tab. VI).

Finally, to further investigate the noise suppression ability of the IMM-PSO strategy, other experiments have been carried out. Towards this end, the inversion results, when the synthetic data are corrupted by increasing the amount of random additive gaussian noise, are shown in Fig. 16. As can be noted by comparing the error values reported in Fig. 16 with those in Tab. IV (related to a homogeneous scatterer), the performance of the IMM-PSO gets worse because of the more complex scatterer under test. The most relevant effect of the increase of the noise level appears to be a significant reduction of the quantitative imaging capabilities ($\varepsilon_{int}^{(IMM-PSO)}\Big|_{Noiseless} = 4.78$ vs. $\varepsilon_{int}^{(IMM-PSO)}\Big|_{SNR=5\,dB} = 19.12$), which causes a worse localization ($\rho^{(IMM-PSO)}\Big|_{Noiseless} = 1.80 \times 10^{-3}$ vs. $\rho^{(IMM-PSO)}\Big|_{SNR=5\,dB} = 1.30 \times 10^{-1}$). However, it should be pointed out that $\varepsilon_{tot}^{(IMM-PSO)}\Big|_{s=S^{opt}} < 10.0$ whatever the SNR value.

4.3 Experimental Validation

In order to complete the validation of the imaging procedure based on the PSO, let us consider the inversion of experimental data as measured by the Institute Fresnel, Marseille, France [38].

The experimental set-up consists of a fixed emitter (a double-ridged horn transmitting antenna) and a receiver rotating, with a mechanical support, around the vertical axis of scatterer under test. The probing antenna illuminates the object from $V = 36$ different locations equally-spaced in a circle $R_O = 720\,mm \pm 3\,mm$ in radius. Due to the physical limitations, the scattered field is measured in $M_{(v)} = 49$ points for each illumination angle. Since the longitudinal dimension of the targets, a two-dimensional electromagnetic imaging model is allowed. A detailed description of the underlying experimental setup together with the complete dataset can be found in the introduction of [39] (pp. 1565-1572) by Belkebir and Saillard.

The considered experimental dataset ("dielTM_dec8f.exp") is related to an off-centered homogeneous circular cylinder $d = 30\,mm$ in diameter. Such an object is characterized by a nominal value of the object function equal to $\tau(x, y) = 2.0 \pm 0.3$ and it is located at $x_c = 0.0$, $y_c = -30\,mm$. As far as the investigation domain D_I is concerned, a square domain $30 \times 30\,cm^2$ is assumed. Because of the aspect-limited nature of the experimental setup, the complete set of measures has been used, but only mono-frequency data ($f = 4\,GHz$) have been considered.

For the reconstruction, the IMM-PSO strategy has been applied ($I = 100$) and the obtained results have been compared with those achieved in [40] where the IMM was used in combination with the CG-based approach.

Figs. $17(a)$-$17(c)$ show the evolution of the reconstructed profile during the multi-step procedure starting from the free-space configuration ($\tau_n\rfloor_{s=0} = \tau_0$ and $\psi_n^{(v)}\Big\rfloor_{s=0} = E_{inc}^v(x_n, y_n)$). At the end of the optimization process $s = S_{opt} = 3$, the cylinder is correctly located and reconstructed. Moreover, the retrieved values of the scatterer pa-

rameters, if compared to those obtained when the IMM-CG strategy is used [17(*d*)], point out an improvement in the reconstruction accuracy ($\widetilde{x}_c^{(IMM-PSO)} = -1.10\,mm$ vs. $\widetilde{x}_c^{(IMM-CG)} = -1.78\,mm$ and $\widetilde{y}_c^{(IMM-PSO)} = -30.20\,mm$ vs. $\widetilde{y}_c^{(IMM-CG)} = -26.15\,mm$ - Tab. VII).

5 Conclusions

In this paper, a new approach to microwave imaging in the spatial domain has been presented. The approach has been formulated as a global nonlinear optimization problem and a customized PSO has been applied. In such a framework, the use of a PSO has allowed an effective treatment of a complete nonlinear formulation exhibiting a number of interesting features (discussed in Section 1). Consequently, the method has proven to be more efficient for microwave imaging purposes than CG and GA-based methods since it combines the capabilities of a global optimizer in escaping local minima and the convergence speed of a deterministic procedure. The limits of the PSO-based approach in reconstructing a two-dimensional scenario probed by an electromagnetic field have been explored and the results have been very promising. They have shown that the algorithm is robust, handling noisy as well as limited data very well without a significant increase of the computational burden. Moreover, during an exhaustive numerical analysis, it has been pointed out how the integration of the nonlinear optimizer with the IMM strategy could have a remarkable effect on the reconstruction.

However, the proposed scheme can be further improved and future works will be carried out in three different directions and at different levels of the imaging procedure. As far as the minimization is concerned, the convergence rate of the numerical process could strongly benefit of an accurate study of the scheduling of the inertial weight during the iterative procedure to fully exploit the hybrid (i.e., local and global optimization properties) nature of the PSO. In the light of an increase of the convergence rate, the capability of including *a-priori* information in the computational technique is also of fundamental

importance and the definition of a suitable threshold in the swarm velocity seems to be particularly suited for this purpose. Moreover, the simplicity and reduced computational requirements offer hope that the IMM-PSO strategy will provide a feasible approach to three-dimensional inversion problems. Toward this aim, an extension of the proposed method to a full three-dimensional scenario is currently under development.

Acknowledgements

The authors wish to thank E. Vico for useful discussions on PSO, and Ing. D. Residori and N. Arnoldi for kindly providing some numerical results of computer simulations.

References

[1] J. C. Bolomey, "Microwave diffraction tomography for biomediacal applications," *IEEE Trans. Microwave Theory Tech*niques, vol. 30, pp. 1998-2000, November 1982.

[2] J. C. Bolomey, "Recent European developments in active microwave for industrial, scientific and medical applications," *IEEE Trans. Microwave Theory Tech*niques, vol. 37, pp. 2109-2117, June 1989.

[3] S. R. H. Hoole *et al.,* "Inverse problem methodology and finite elements in the identifications of cracks, sources, materials, and their geometry in inaccesible locations," *IEEE Trans. Magn.*, vol. 27, pp. 3433-3443, 1991.

[4] S. Caorsi, A. Massa, M. Pastorino, and M. Donelli, "Improved microwave imaging procedures for nondestructive evaluations of two-dimensional structures," *IEEE Trans. Antennas Propagat.*, vol. 52, no. 6, pp. 1386-1397, June 2004.

[5] A. C. Dubay *et al.,* "Detection technologies for mines and minelike targets," in *Proc. SPIE*, vol. 2496, Orlando, FL, 1995.

[6] R. E. Kleinman and P. M. van den Berg, "An extended range modified gradient technique for profile inversion," *Radio Science*, vol. 28, pp. 877-884, 1993.

[7] K. Belkebir, R. E. Kleinman, and C. Pichot, "Microwave imaging - Location and shape reconstruction from multifrequency scattering data," *IEEE Trans. on Microwave Theory and Techniques*, vol. 45, pp. 469-76, 1997.

[8] H. Harada, D. J. N. Wall, T. Takenaka, and M. Tanaka, "Conjugate gradient method applied to inverse scattering problem," *IEEE Trans. on Antennas and Propagation*, vol. 43, pp. 784-792, 1995.

[9] A. Massa, "Genetic algorithm based techniques for 2D microwave inverse scattering," in *Recent Research Developments in Microwave Theory Tech.*, S. G. Pandalai Ed., Trivandrum, India: Transworld Res. Network Press, 2002.

[10] R. E. Kleinman and P. M. van den Berg, "A modified gradient method for two-dimensional problems in tomography," *J. Computat. Appl. Math.*, vol. 42, pp. 17-35, 1992.

[11] P. M. van den Berg and R. E. Kleinman, "A contrast source inversion method," *Inverse Problems*, vol. 13, pp. 1607-1620, 1997.

[12] Z. Q. Meng, T. Takenaka, and T. Tanaka, "Image reconstruction of two-dimensional impenetrable objects using genetic algorithm," *J. Electromagn. Waves Applicat.*, vol. 13, pp. 95-118, 1999.

[13] M. Pastorino, A. Massa, and S. Caorsi, "A microwave inverse scattering technique for image reconstruction based on a genetic algorithm," *IEEE Trans. on Instrumentation and Measurement*, vol. 49, pp. 573-578, 2000.

[14] H. K. Choi, S. K. Park, and J. W. Ra, "Reconstruction of a high-contrast penetrable object in pulsed time domain by using the genetic algorithm," *Proc. 1997 IEEE Int. Geoscience and Remote Sensing Symp.*, Singapore, Aug. 1997, pp. 136-138.

[15] J. Kennedy and R. C. Eberhart, "Particle swarm optimization," in *Proc. IEEE Int. Conference Neural Networks*, vol. IV, Perth, Australia, November/December 1995, pp. 1942-1948.

[16] J. Robinson, S. Sinton, and Y. Rahmat-Samii, "Particle swarm, genetic algorithm, and their hybrids: Optimization of a profiled corrugated horn antenna," in *IEEE Antennas Propagat. Soc. Int. Symp. Dig.*, vol. 1, pp. 314-317, 2002.

[17] D. Gies and Y. Rahmat-Samii, "Particle swarm optimization for reconfigurable phase-differentiated array design," *Microwave and Optical Technology Letters*, vol. 38, no. 3, 2003.

[18] D. W. Boringer and Douglas H. Werner, "Particle swarm optimization versus genetic algorithms for phased array synthesis," *IEEE Trans. Antennas Propagat.*, vol. 52, no. 3, pp. 771-779, March 2004.

[19] J. R. Robinson and Y. Rahmat-Sami, "Particle swarm optimization in electromagnetics," *IEEE Trans. Antennas Propagat.*, vol. 52, no. 3, pp. 771-778, March 2004.

[20] D. Colton and R. Krees, *Inverse acoustics and electromagnetic scattering theory.* Berlin, Germany: Springer-Verlag, 1992.

[21] J. H. Richmond, "Scattering by a dielectric cylinder of arbitrary cross section shape," *IEEE Trans. Antennas Propagat.*, vol. 13, pp. 334-341, May 1965.

[22] J. Kennedy, R. C. Eberhart, and Y. Shi, *Swarm Intelligence.* San Francisco: Morgan Kaufmann Publishiers, 2001.

[23] M. Clerk and J. Kennedy, "The Particle Swarm-Explosion, Stability, and Convergence in a Multidimensional Complex Space," *IEEE Trans. Evolutionary Computation*, vol. 6, pp. 58-73, 2002.

[24] A. Carlisle and G. Doizier, "An off-the-shelf PSO," in *Proc. Workshop Particle Swarm Optimization*, Purdue School of Engineering and Technology, Indianapolis, 2001.

[25] R. C. Eberhart and Y. Shi, "Particle Swarm Optimization: Developments, Applications and Resources," *Proc. Congress on Evolutionary Computation 2001,* Seul, Corea, pp. 81-86, 2001.

[26] R. C. Eberhart and Y. Shi, "Comparing inertia weights and constriction factors in particle swarm optimization," in *Proc. Congress on Evolutionary Computation 2000,* Piscataway, USA, pp. 84-88, 2000.

[27] Y. Shi and R. C. Eberhart, "Empirical study of particle swarm optimization," in *Proc. Congress on Evolutionary Computation 1999,* Washington, USA, pp. 1945-1950, 1999.

[28] F. van den Berg and A. P. Engelbrecht, "Effect of swarm size on cooperative particle swarm optimizers," in *Proc. Evolutionary Computation Conference GECCO-2001,* San Francisco, USA, pp. 892-899, 2001.

[29] Y. Shi and R. Eberhart, "A modified particle swarm optimizer," in *Proc. IEEE world Congr. Computational Intelligence Evolutionary Computation*, pp. 69-73, 1998.

[30] A. I. El-Gallad, M. El-Hawary, A. A. Sallam, and A. Kalas, "Swarm intelligence for hybrid cost dispatch problem," in *Proc. Canadian Conference Electrical and Computer Engineering*, vol. 2, pp. 753-757, 2001.

[31] S. Caorsi, M. Donelli, D. Franceschini, and A. Massa, "A new methodology based on an iterative multiscaling for microwave imaging," *IEEE Trans. Microwave Theory Tech.*, vol. 51, pp. 1162-1173, April 2003.

[32] D. S. Jones, *The Theory of the Electromagnetism.* Pergamon Press, New York, 1964.

[33] R. V. Kohn and A. McKenney, "Numerical implementation of a variational method for electrical impedance tomography," *Inverse Problems*, vol. 6, pp. 389-414, 1990.

[34] S. Caorsi, A. Massa, and M. Pastorino, "A computational technique based on a real-coded genetic algorithm for microwave imaging purposes," *IEEE Trans. Geoscience and Remote Sensing*, special issue on "Computational Wave Issues in Remote Sensing, Imaging and Target Identification, Propagation, and Inverse Scattering," vol. 38, n. 4, part I, pp. 1697-1708, July 2000.

[35] D. E. Goldberg, *Genetic Algorithms in Search, Optimization, and Machine Learning.* Addison-Wesley, Reading, Mass., 1989.

[36] O. M. Bucci and G. Franceschetti, "On the degrees of freedom of scattered fields," *IEEE Trans. Antennas Propagat.*, vol 37, pp 918-926, July 1989.

[37] S. Caorsi, M. Donelli, and A. Massa, "Location, detection, and imaging of multiple scatterers by means of the iterative multiscaling method", *IEEE Trans. Microwave Theory Tech.*, vol. 52, pp. 1217-1228, 2004.

[38] K. Belkebir, S. Bonnard, F. Sabouroux, and M. Saillard, "Validation of 2D inverse scattering algorithms from multi-frequency experimental data," *J. Electromagn. Waves Appl.*, vol. 14, pp. 1637-1668, 2000.

[39] K. Belkebir and M. Saillard, "Testing Inversion algorithms against experimental data," *Inverse problems*, vol. 17, pp. 1565-1702, 2001.

[40] S. Caorsi, Massimo Donelli, and A. Massa, "Analysis of the stability and robustness of the iterative multi-scaling approach for microwave imaging applications," *Radio Science,* (in press).

Figure Captions

- Figure 1. Reference problem geometry.
- Figure 2. *PSO-based* procedure - Block diagram.
- Figure 3. *Calibration process* - Behavior of the average optimal cost function value versus the swarm dimension, I.
- Figure 4. *Calibration process* - Behavior of the average optimal cost function value versus the value of the inertial weight w.
- Figure 5. *Calibration process* - Behavior of the average optimal cost function value versus the *cognitive* and *social* scaling (or accelerations) parameters, C_1 and C_2.
- Figure 6. Reconstruction of an off-centered homogeneous ($\tau = 2.0$) circular ($d = 0.3\,\lambda_0$) cylinder by means of (a) *PSO-based* procedure, (b) *CG-based* procedure, and (c) *GA-based* procedure. Ideal reconstruction (d).
- Figure 7. Reconstruction of an off-centered homogeneous ($\tau = 2.0$) circular ($d = 0.3\,\lambda_0$) cylinder - Behavior of the cost function $\phi^{(k)}$ versus the iteration number k during the minimization process.
- Figure 8. Reconstruction of an off-centered homogeneous ($\tau = 2.0$) circular ($d = 0.3\,\lambda_0$) cylinder (Noisy Data) - *PSO-based* procedure: values of the error figures related to (a) the *qualitative imaging* accuracy and to (b) the *quantitative imaging* accuracy versus SNR.
- Figure 9. Reconstruction of an off-centered homogeneous ($\tau = 2.0$) circular ($d = 0.3\,\lambda_0$) cylinder - Reference profile (a). *IM* method and *PSO-based* procedure (IMM-PSO): reconstructed profile at (b) $s = 1$, (c) $s = 2$, and (d) $s = S^{opt} = 3$.
- Figure 10. Reconstruction of a centered homogeneous ($\tau = 0.5$) square ($L = 0.8\,\lambda_0$) cylinder - Reference profile (a). *IM* method and *PSO-based* procedure (IMM-PSO):

reconstructed profile at (b) $s = 1$, (c) $s = 2$, and (d) $s = S^{opt} = 3$.

- Figure 11. Reconstruction of a centered homogeneous ($\tau = 0.5$) square ($L = 0.8\,\lambda_0$) cylinder - *IMM-PSO* strategy: values of the error figures related to (a) the *qualitative imaging* accuracy and to (b) the *quantitative imaging* accuracy versus step number s ($s = 1$, ..., S^{opt}).

- Figure 12. Reconstruction of a centered homogeneous ($\tau = 0.5$) square ($L = 0.8\,\lambda_0$) cylinder - Retrieved profile with the *IM* approach integrated with (a) the *CG-based* procedure (*IMM-CG* strategy) and (b) the *GA-based* procedure (*IMM-GA* strategy).

- Figure 13. Reconstruction of a centered homogeneous ($\tau = 0.5$) square ($L = 0.8\,\lambda_0$) cylinder - *IMM-PSO* strategy: behavior of the cost function $\phi^{(k)}$ versus the iteration number k during the iterative multi-step process.

- Figure 14. Reconstruction of an off-centered hollow square cylinder ($L_{inner} = 0.4\lambda_0$, $L_{outer} = 1.2\lambda_0$, and $\tau = 0.5$) cylinder (Noisy conditions, $SNR = 30\,dB$) - Reference profile (a). Retrieved profile with the *IM* approach integrated with (b) the *PSO-based* procedure (*IMM-PSO* strategy) and (c) the *CG-based* procedure (*IMM-CG* strategy) [31].

- Figure 15. Reconstruction of a centered stratified square cylinder ($L_{inner} = 0.4\lambda_0$, $\tau_{inner} = 2.0$ and $L_{outer} = 1.2\lambda_0$, $\tau_{outer} = 0.5$) cylinder (Noisy conditions, $SNR = 20\,dB$) - Reference profile (a). Retrieved profile with the *IM* approach integrated with (b) the *PSO-based* procedure (*IMM-PSO* strategy) and (c) the *GA-based* procedure (*IMM-GA* strategy). Horizontal cross-section view (d).

- Figure 16. Reconstruction of a centered stratified square cylinder ($L_{inner} = 0.4\lambda_0$, $\tau_{inner} = 2.0$ and $L_{outer} = 1.2\lambda_0$, $\tau_{outer} = 0.5$) cylinder (Noisy conditions, $SNR = 20\,dB$) - *IMM-PSO* strategy: values of the error figures related to (a) the *qualitative imaging* accuracy and to (b) the *quantitative imaging* accuracy versus SNR.

- Figure 17. Reconstruction of an off-centered homogeneous circular cylinder (Real dataset "Marseille" [39] - "dielTM_dec8f.exp" - $f = 4\,GHz$). *IMM-PSO* strategy: reconstructed profile at (a) $s = 1$, (b) $s = 2$, and (c) $s = S^{opt} = 3$. *IMM-CG* strategy: reconstructed profile at the convergence step (d) $s = S^{opt} = 2$ [40].

Table Captions

- Table I. Reconstruction of an off-centered homogeneous ($\tau = 2.0$) circular ($d = 0.3\,\lambda_0$) cylinder. Values of the qualitative (ρ and δ) and quantitative (ε_{tot}, ε_{int}, and ε_{ext}) error figures for *PSO*, *CG*, and *GA*-based procedures.

- Table II. Reconstruction of an off-centered homogeneous ($\tau = 2.0$) circular ($d = 0.3\,\lambda_0$) cylinder. Error figures and iterative-process parameters for the the *IM* approach integrated with the *PSO-based* procedure at different steps s ($s = 1$, ..., S^{opt}) of the multi-scaling procedure.

- Table III. Reconstruction of a centered homogeneous ($\tau = 0.5$) square ($L = 0.8\,\lambda_0$) cylinder. Error figures and iterative-process parameters for the the *IM* approach integrated with the *PSO-based* procedure (*IMM-PSO* strategy), the *CG-based* procedure (*IMM-CG* strategy), and (c) the *GA-based* procedure (*IMM-GA* strategy).

- Table IV. Reconstruction of a centered homogeneous ($\tau = 0.5$) square ($L = 0.8\,\lambda_0$) cylinder (Noisy conditions) - *IMM-PSO* strategy: error figures and iterative-process parameters for various SNR values.

- Table V. Reconstruction of an off-centered hollow square cylinder ($L_{inner} = 0.4\lambda_0$, $L_{outer} = 1.2\lambda_0$, and $\tau = 0.5$) cylinder (Noisy conditions, $SNR = 30\,dB$) [31] - Error figures and iterative-process parameters for the the *IM* approach integrated with the *PSO-based* procedure (*IMM-PSO* strategy) and the *CG-based* procedure (*IMM-CG* strategy) .

- Table VI. Reconstruction of a centered stratified square cylinder ($L_{inner} = 0.4\lambda_0$, $\tau_{inner} = 2.0$ and $L_{outer} = 1.2\lambda_0$, $\tau_{outer} = 0.5$) cylinder (Noisy conditions, $SNR = 20\,dB$) - Error figures and iterative-process parameters for the the *IM* approach integrated with the *PSO-based* procedure (*IMM-PSO* strategy) and the *GA-based* procedure (*IMM-GA* strategy).

- Table VII. Reconstruction of an off-centered homogeneous circular cylinder (Real dataset "Marseille" [39] - "dielTM_dec8f.exp" - $f = 4\,GHz$). Estimated geometric parameters and iterative-process parameters ($x_{c_{(S_{opt})}}$, $y_{c_{(S_{opt})}}$, $L_{(S_{opt})}$ $[mm]$).

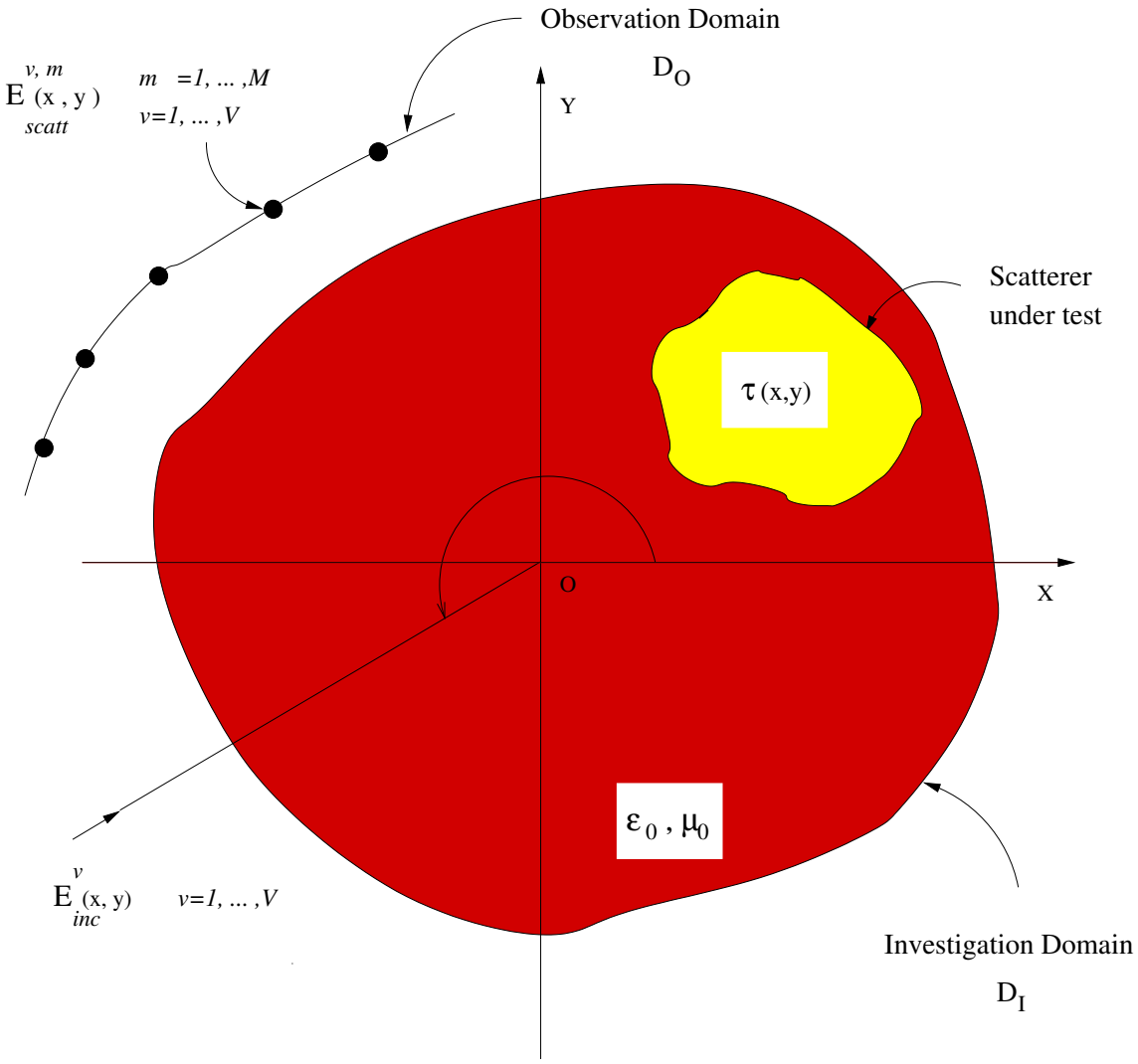

Fig. 1 - M. Donelli *et al.*, "A computational approach based on ..."

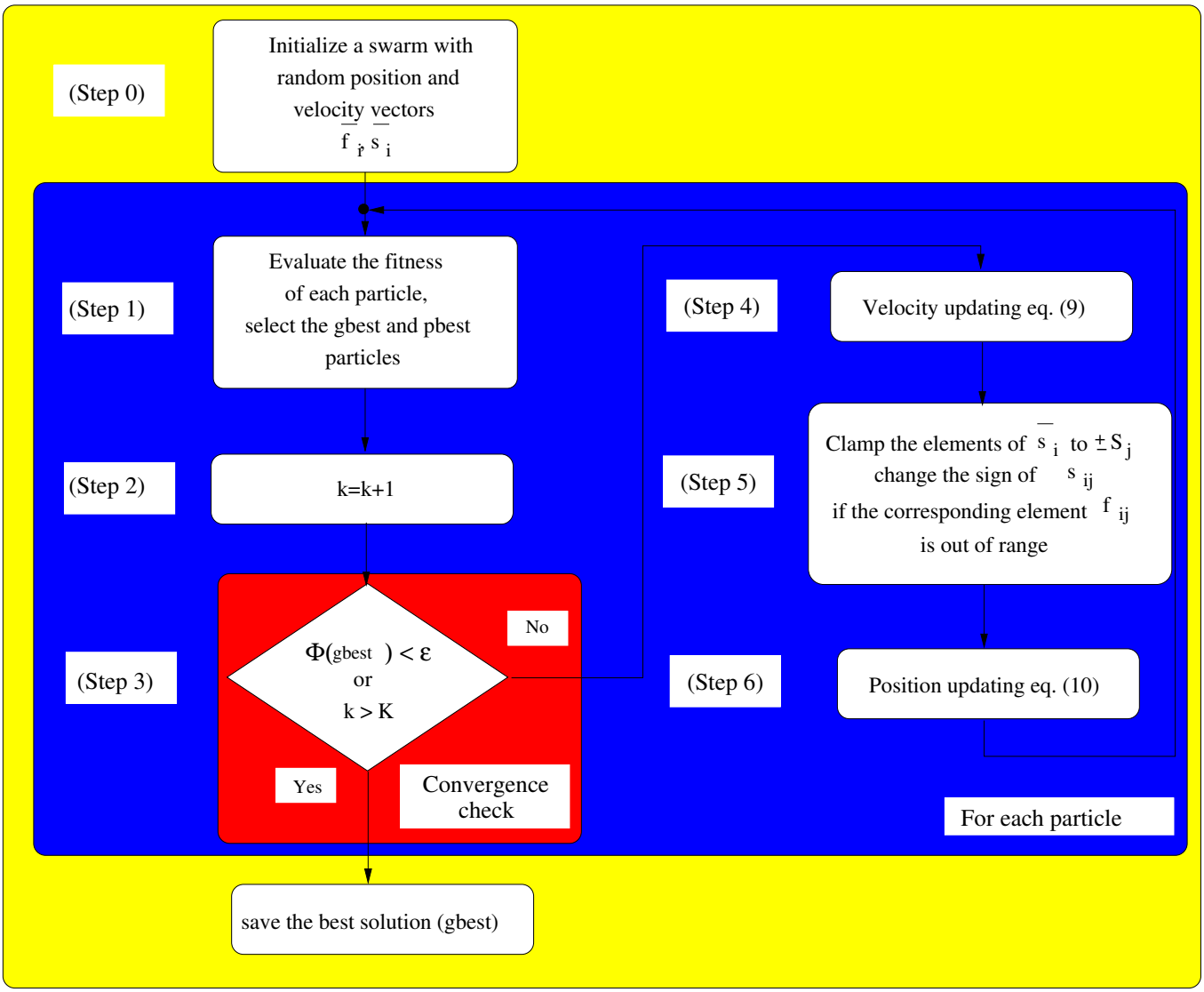

Fig. 2 - M. Donelli *et al.*, "A computational approach based on ..."

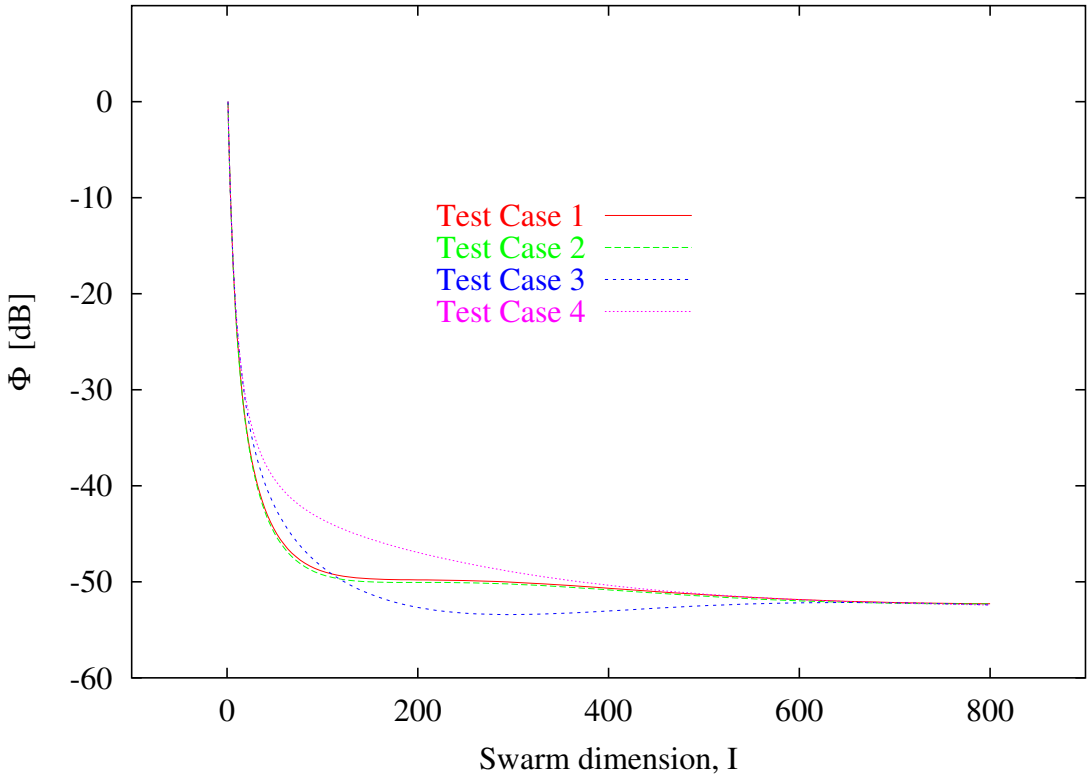

Fig. 3 - M. Donelli *et al.*, "A computational approach based on ..."

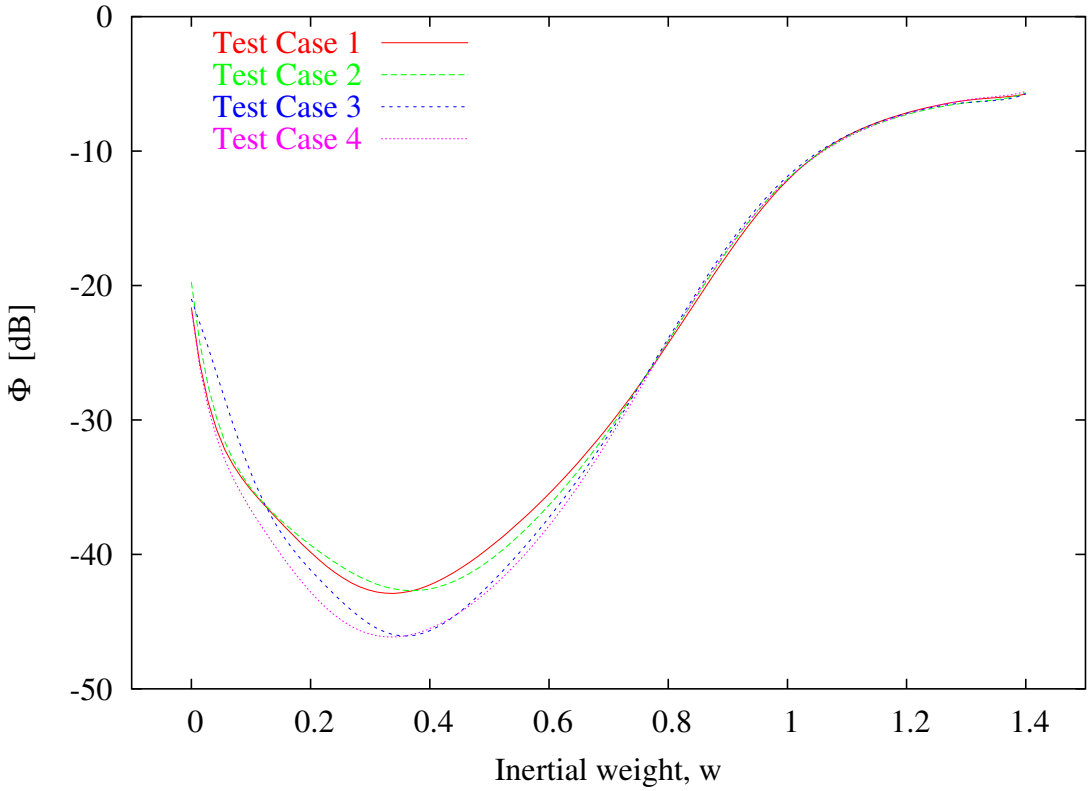

Fig. 4 - M. Donelli *et al.*, "A computational approach based on ..."

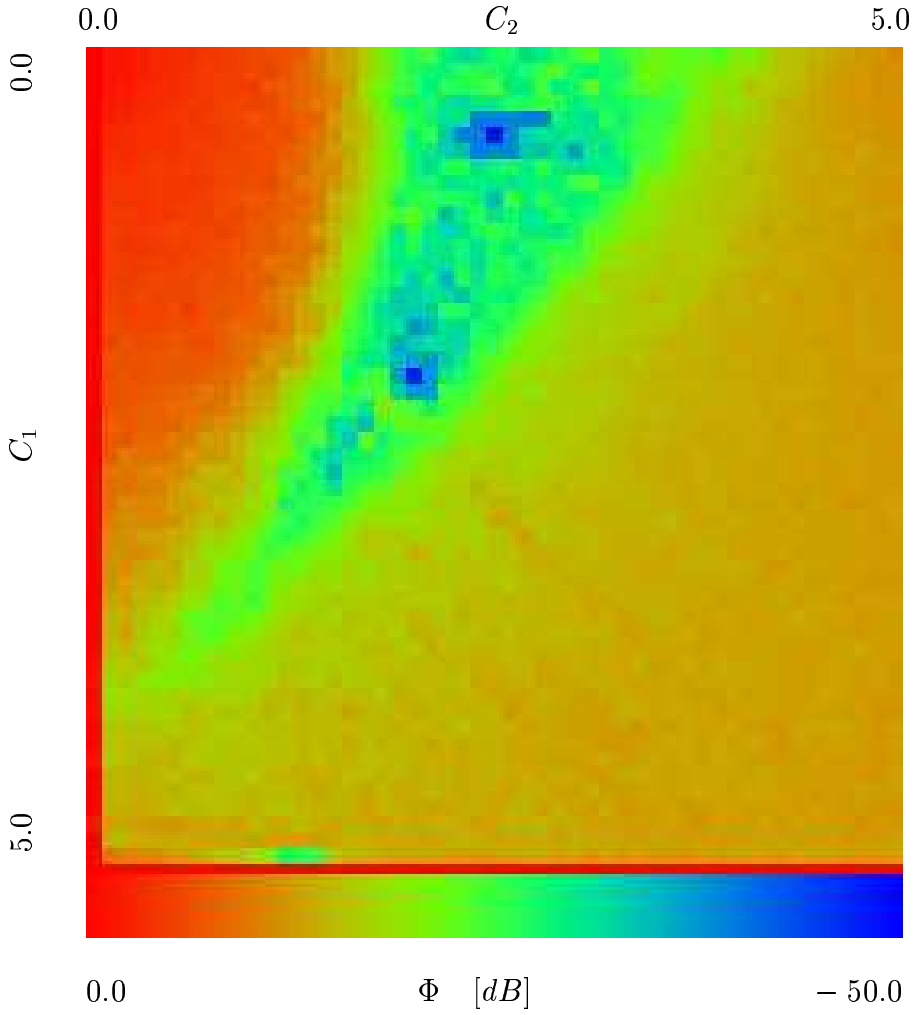

Fig. 5 - M. Donelli *et al.*, "A computational approach based on ..."

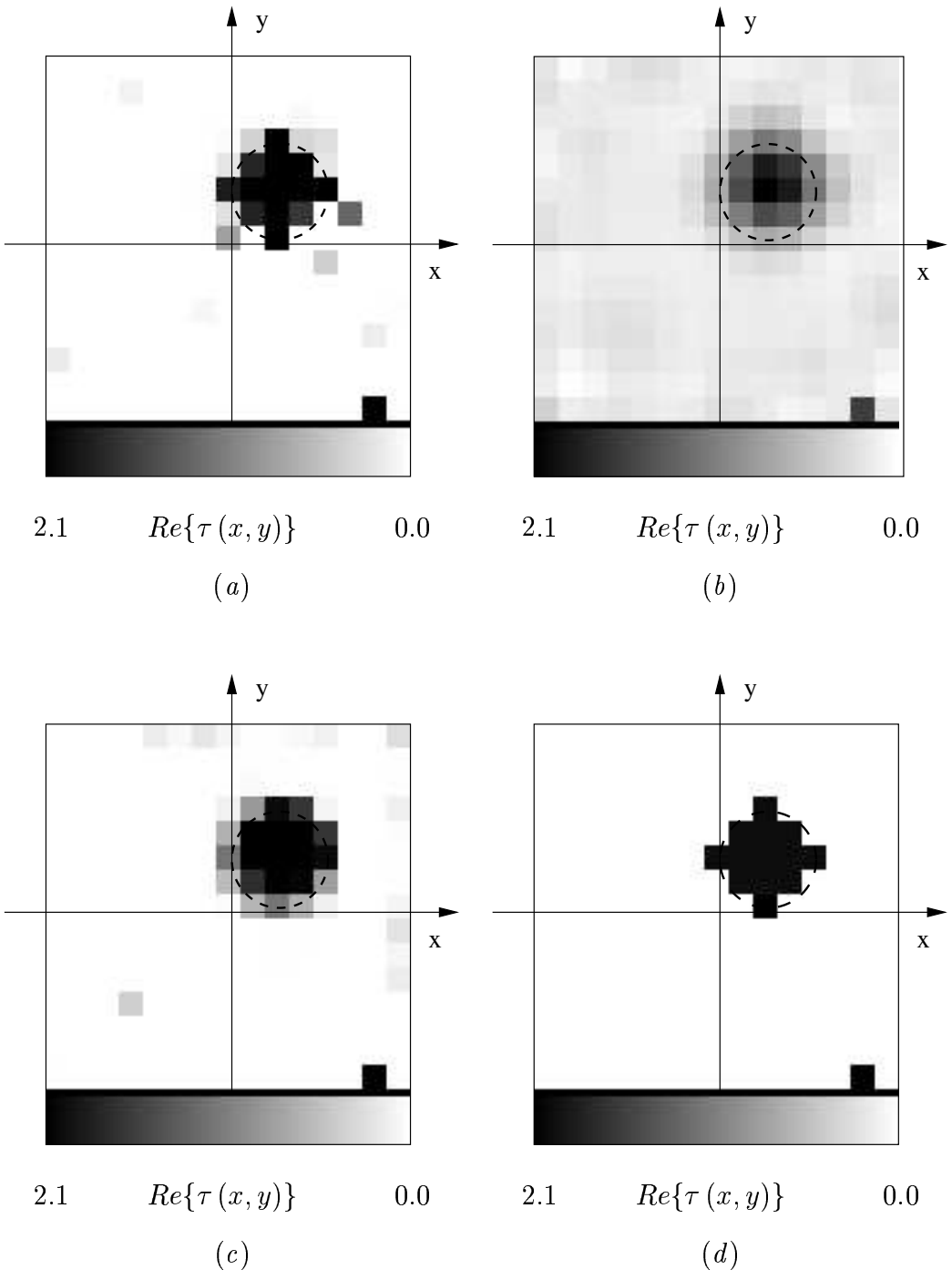

Fig. 6 - M. Donelli *et al.*, "A computational approach based on ..."

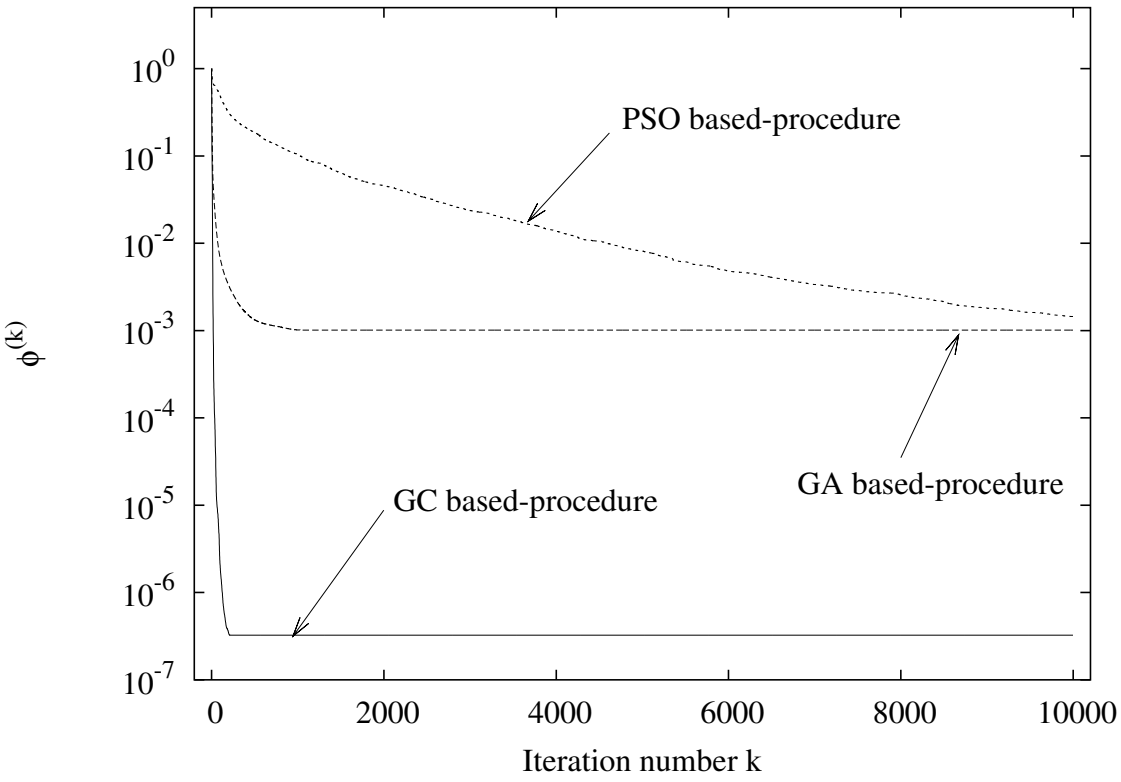

Fig. 7 - M. Donelli *et al.*, "A computational approach based on ..."

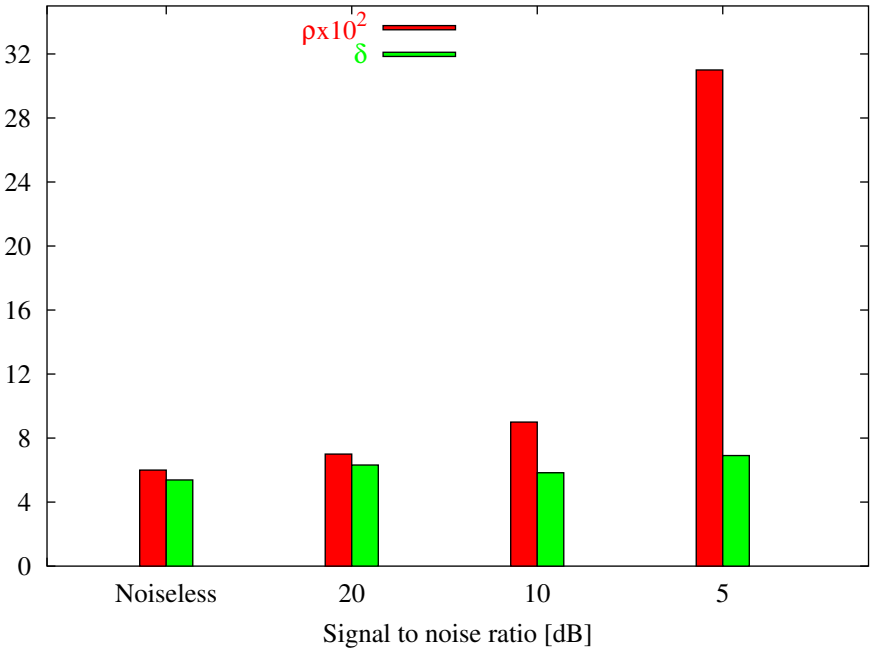

(a)

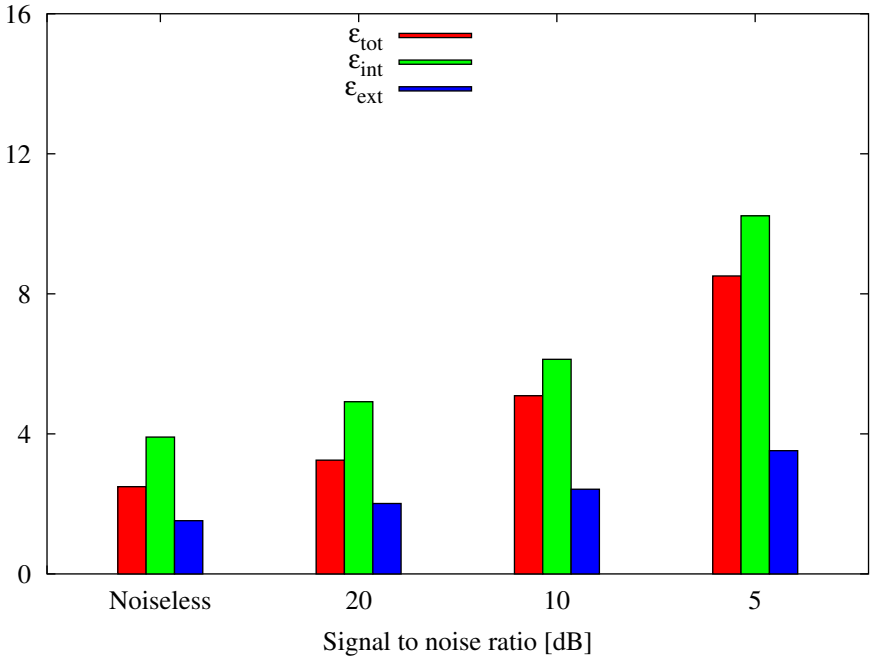

(b)

Fig. 8 - M. Donelli *et al.*, "A computational approach based on ..."

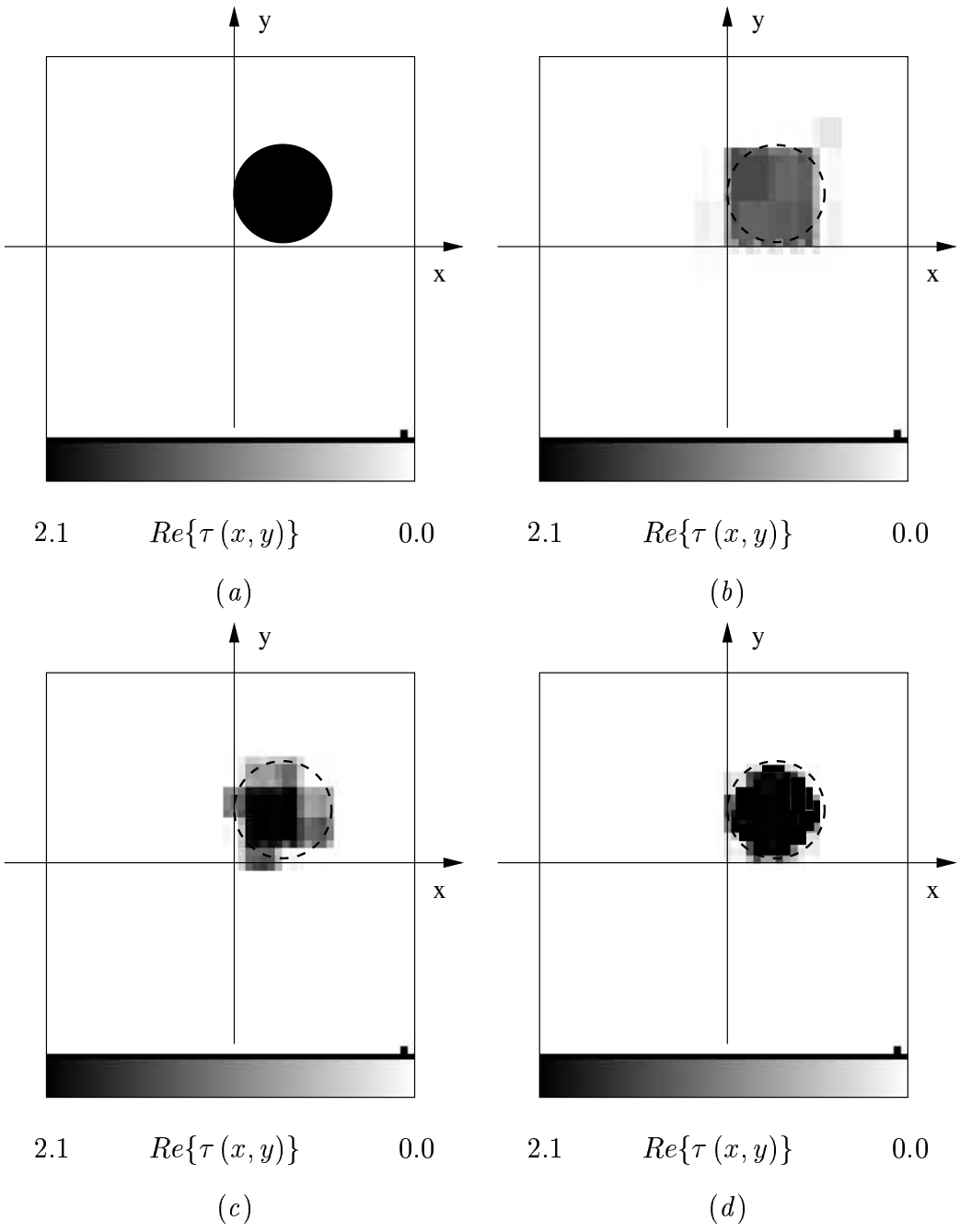

Fig. 9 - M. Donelli *et al.*, "A computational approach based on ..."

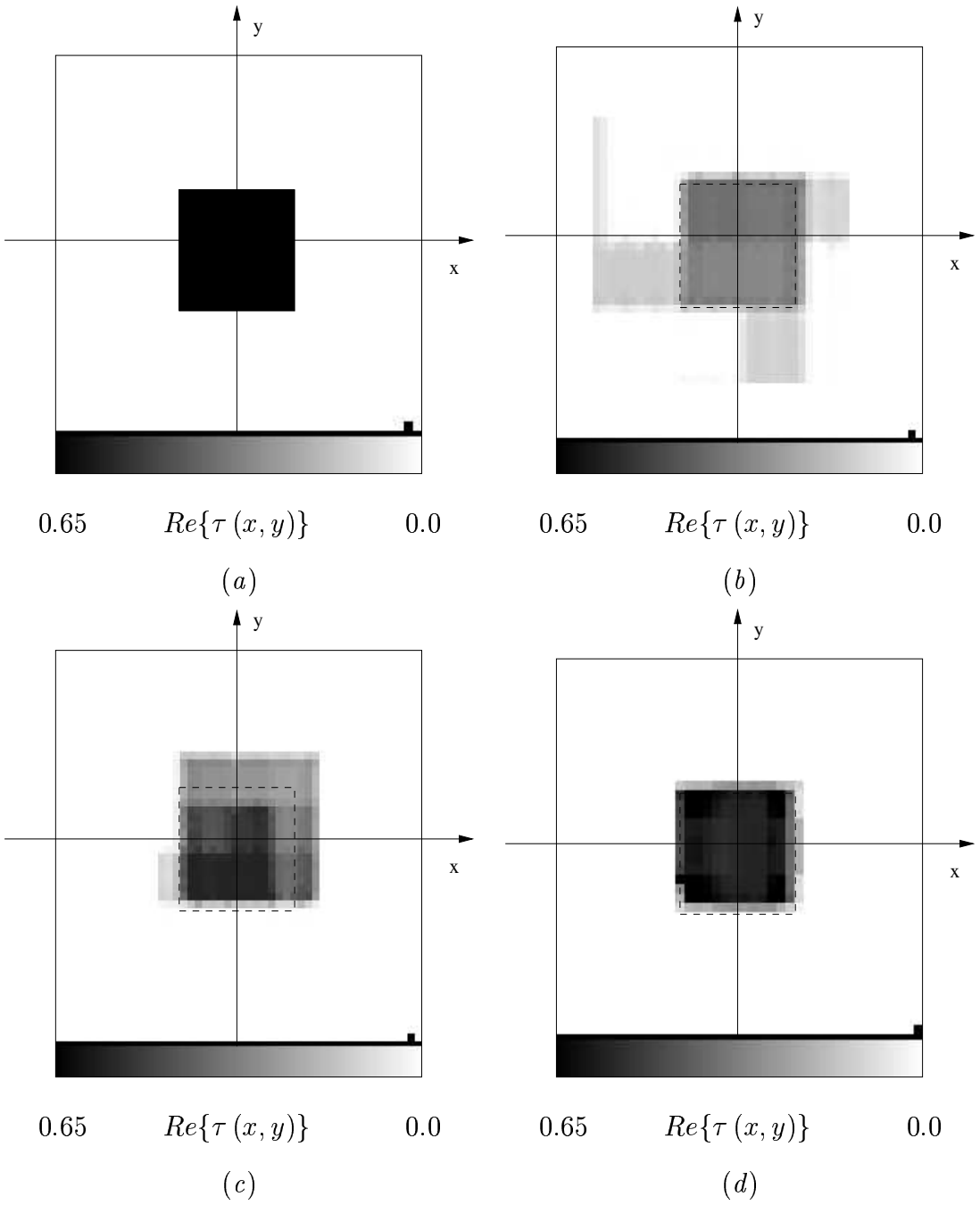

Fig. 10 - M. Donelli *et al.*, "A computational approach based on ..."

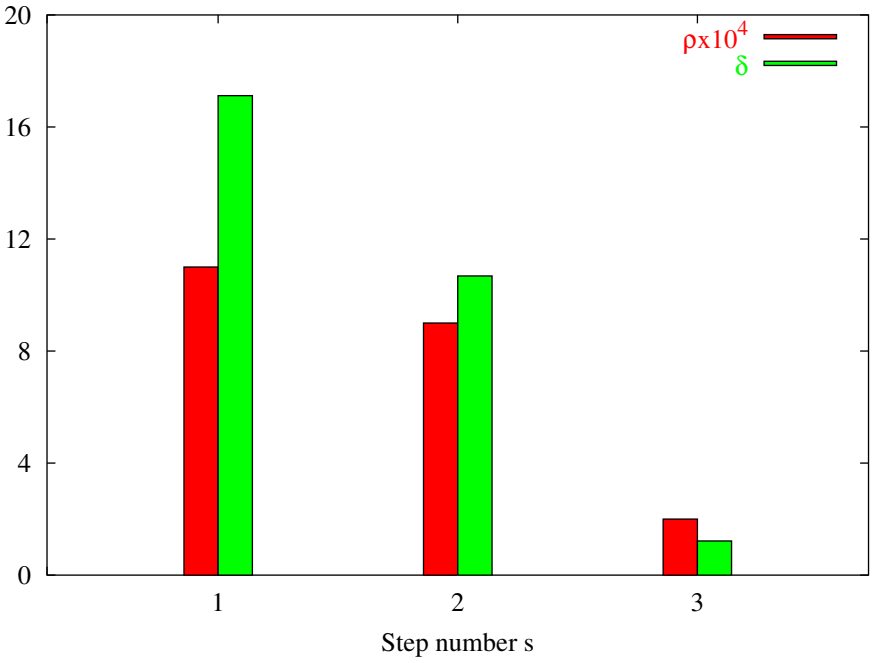

(a)

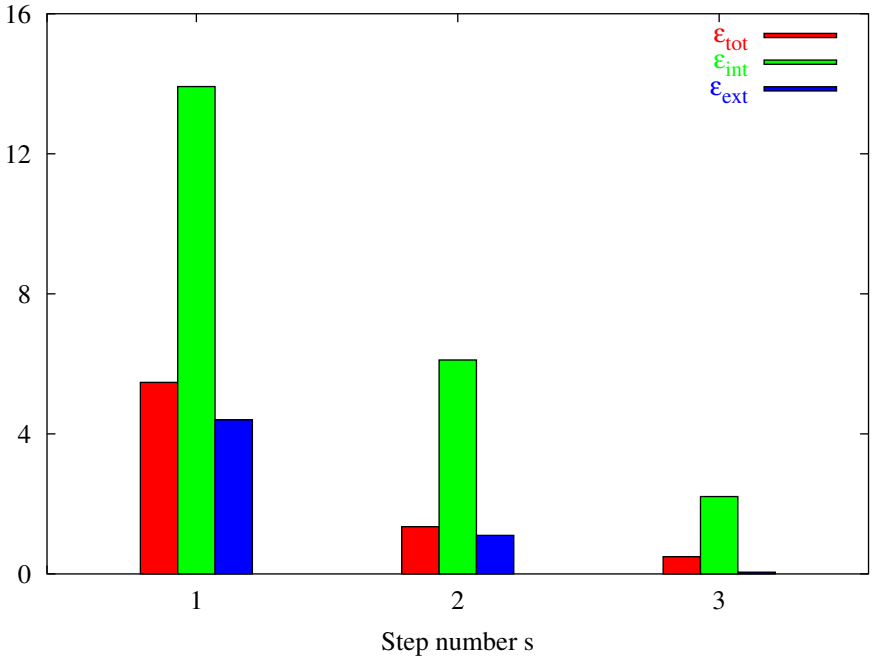

(b)

Fig. 11 - M. Donelli *et al.*, "A computational approach based on ..."

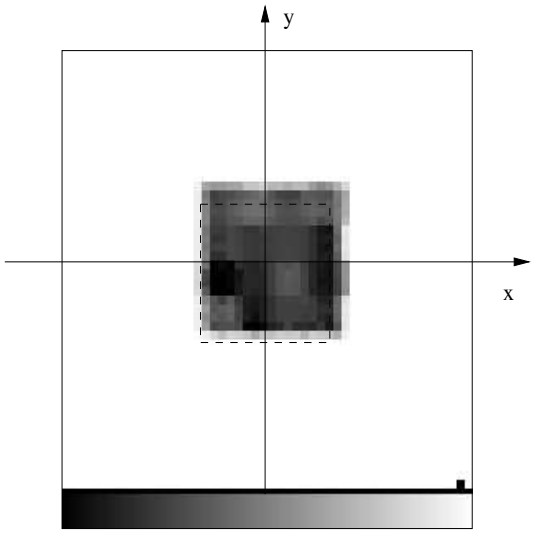

0.65 $Re\{\tau\,(x,y)\}$ 0.0

(a)

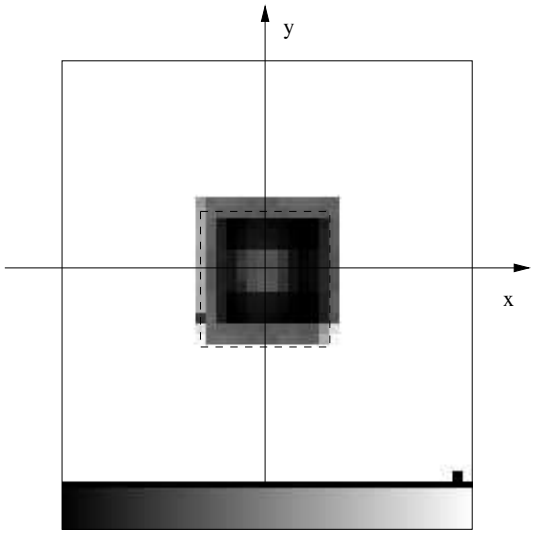

0.65 $Re\{\tau\,(x,y)\}$ 0.0

(b)

Fig. 12 - M. Donelli *et al.*, "A computational approach based on ..."

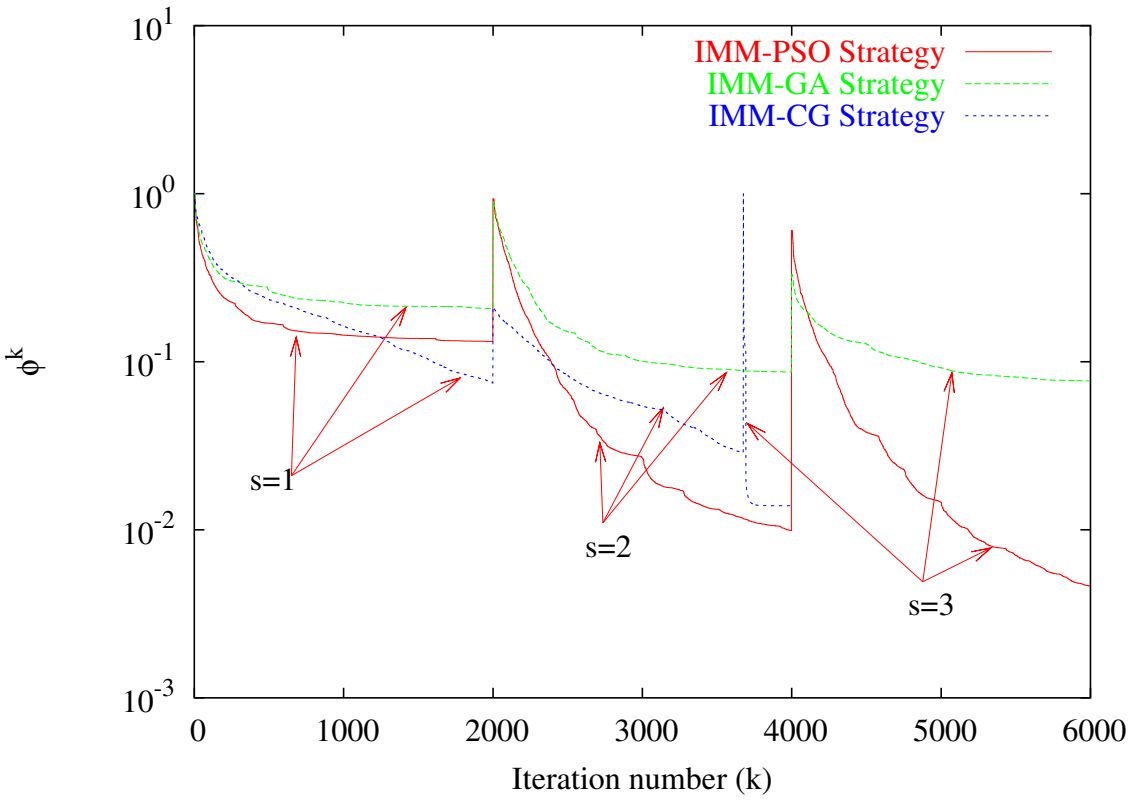

Fig. 13 - M. Donelli *et al.*, "A computational approach based on ..."

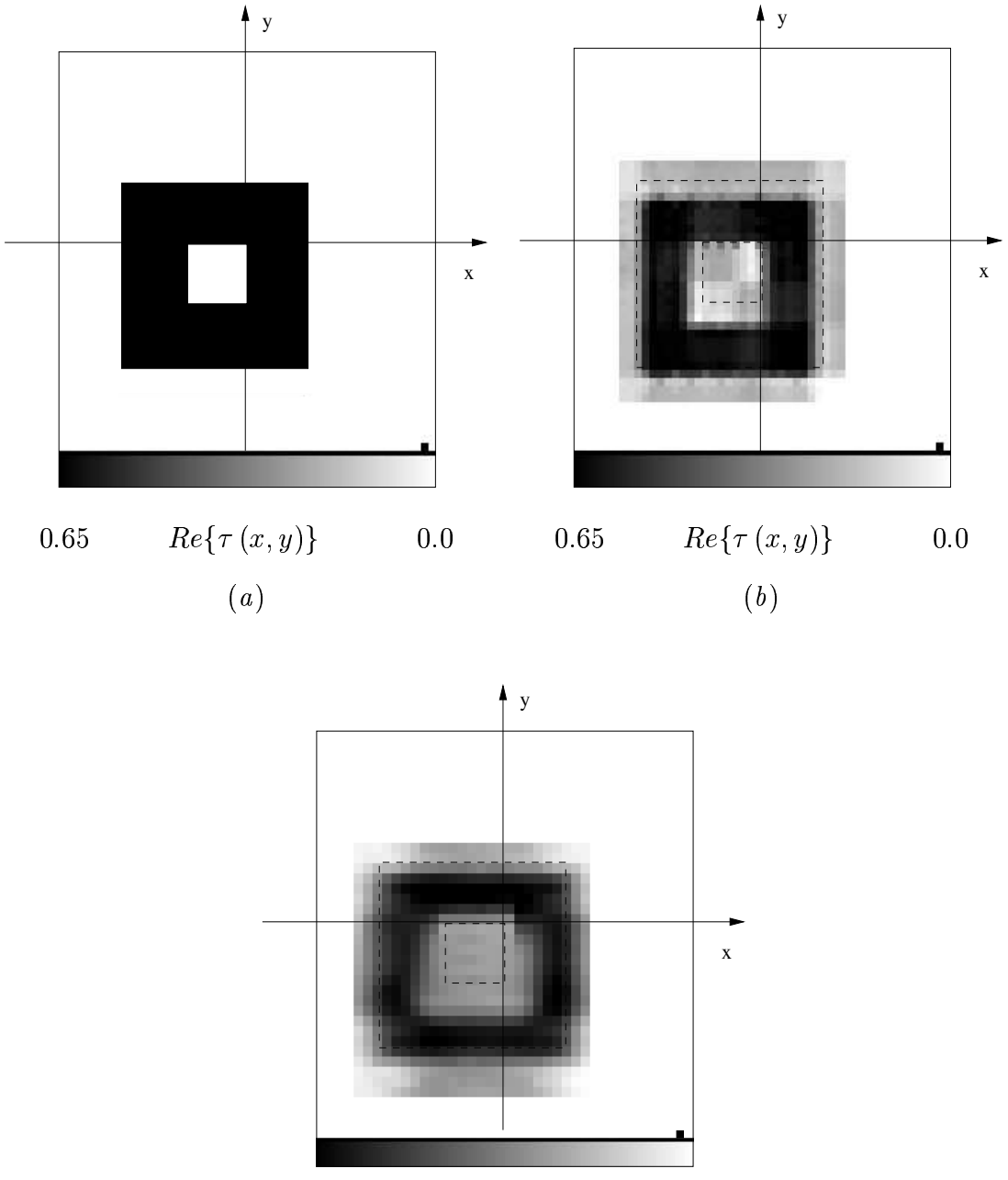

Fig. 14 - M. Donelli *et al.*, "A computational approach based on ..."

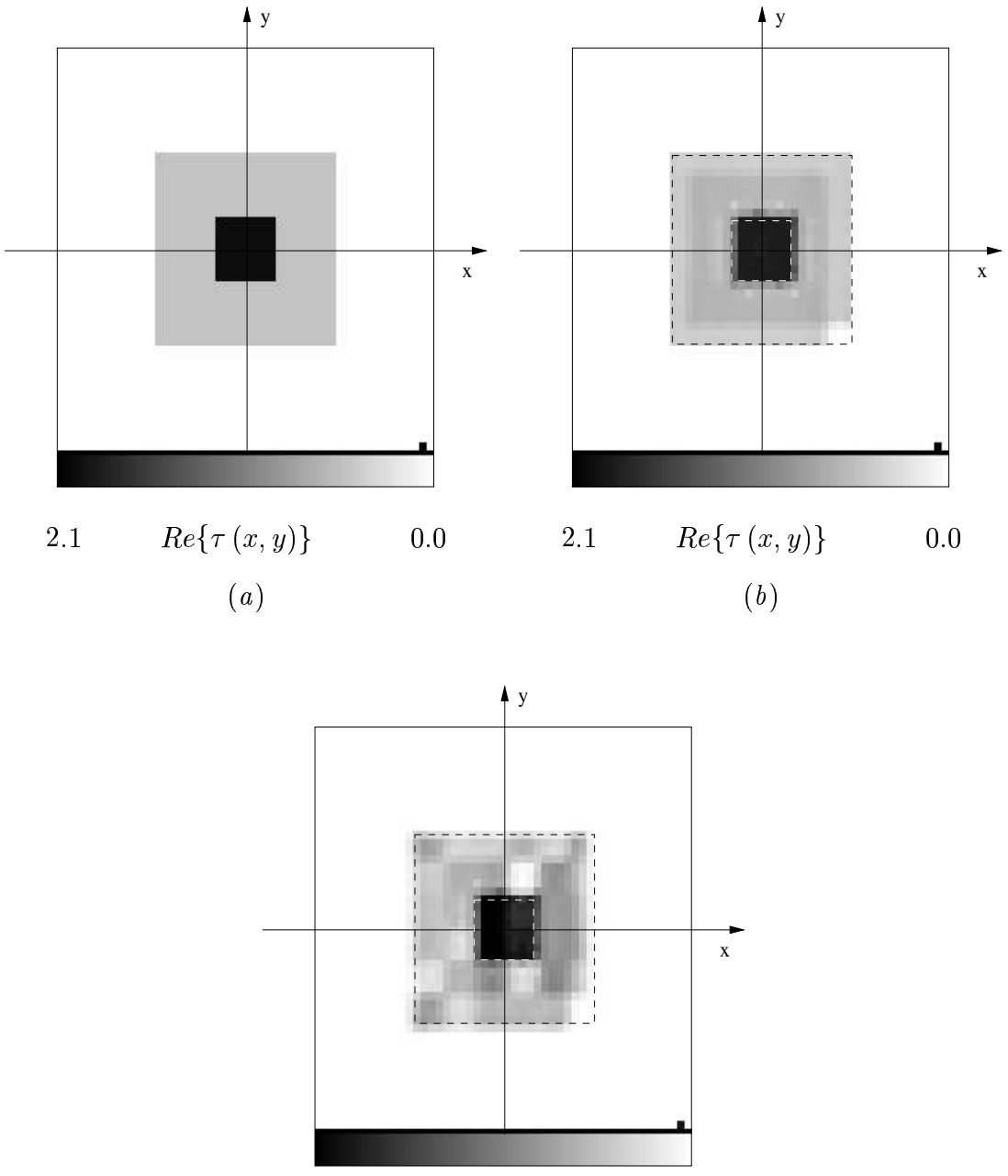

Fig. 15(I) - M. Donelli *et al.*, "A computational approach based on ..."

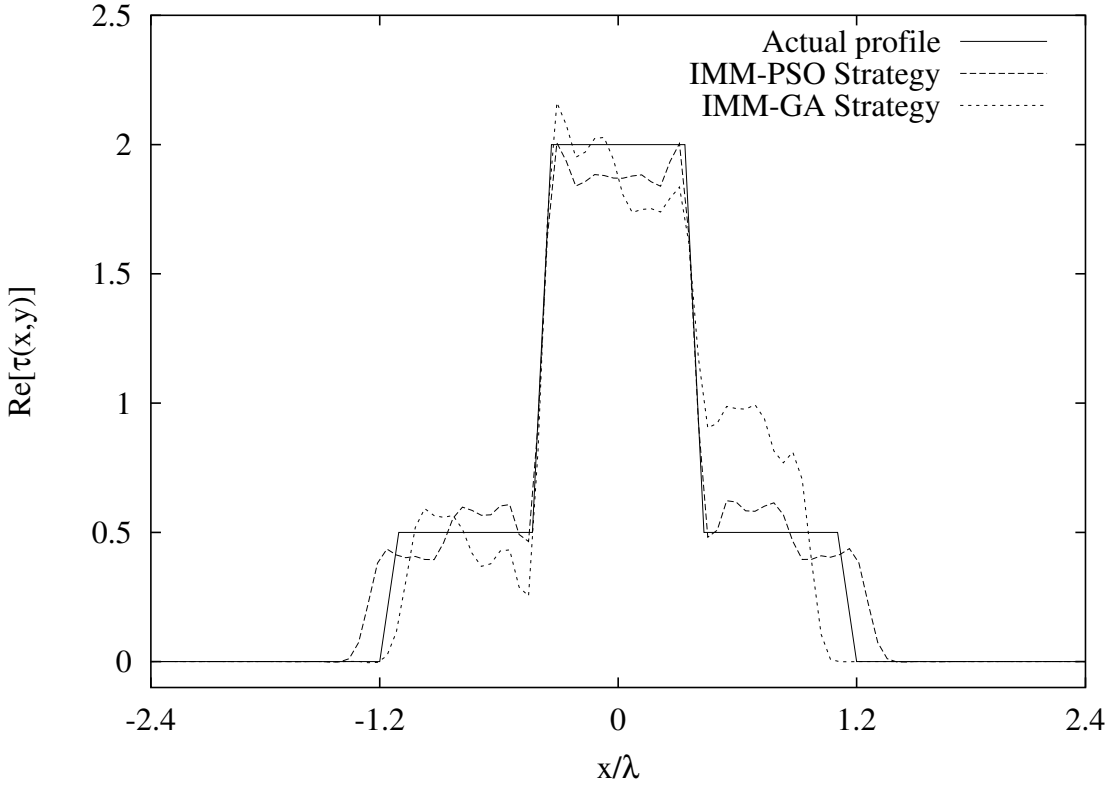

(d)

Fig. 15(*II*) - M. Donelli *et al.*, "A computational approach based on ..."

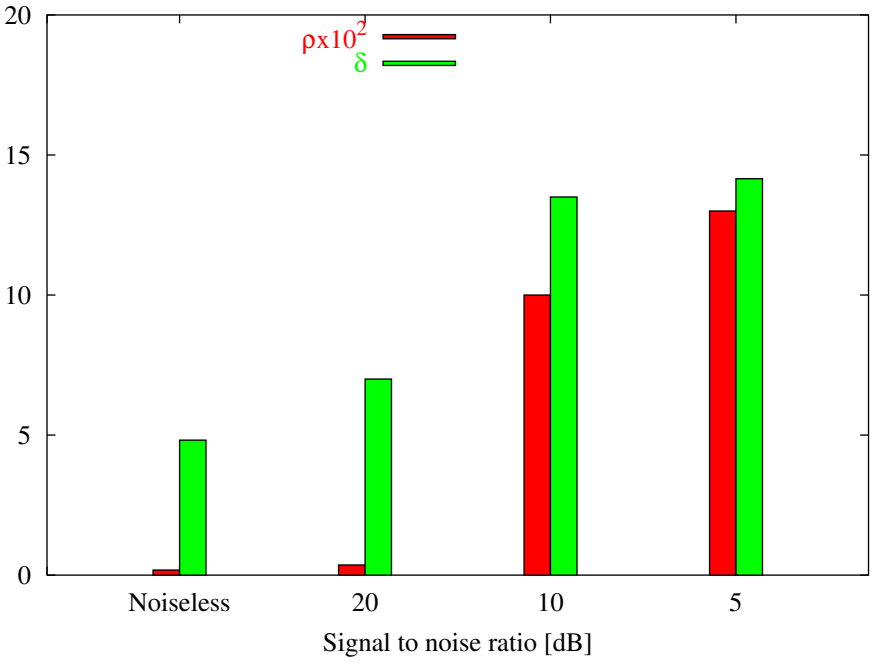

(a)

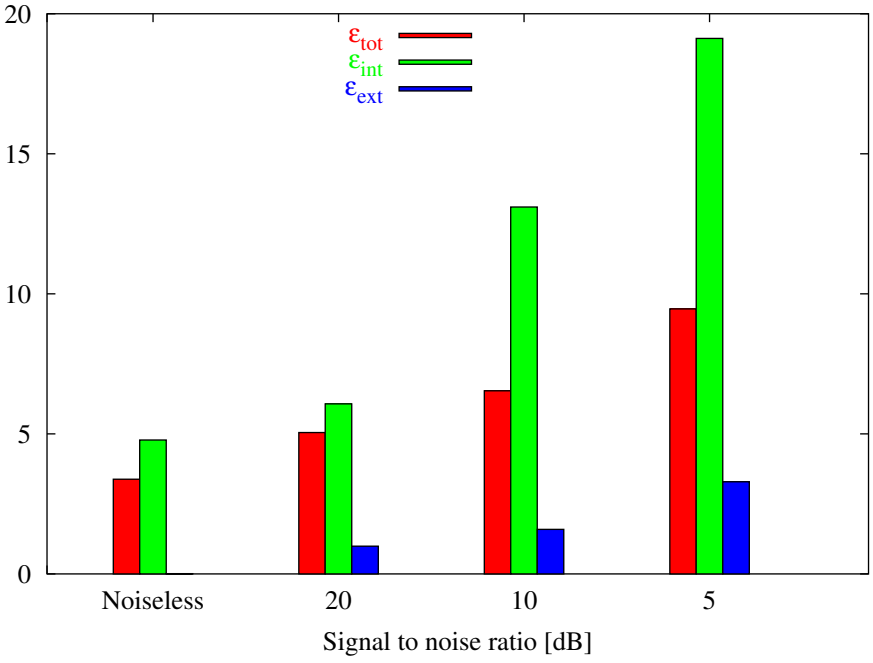

(b)

Fig. 16 - M. Donelli *et al.*, "A computational approach based on ..."

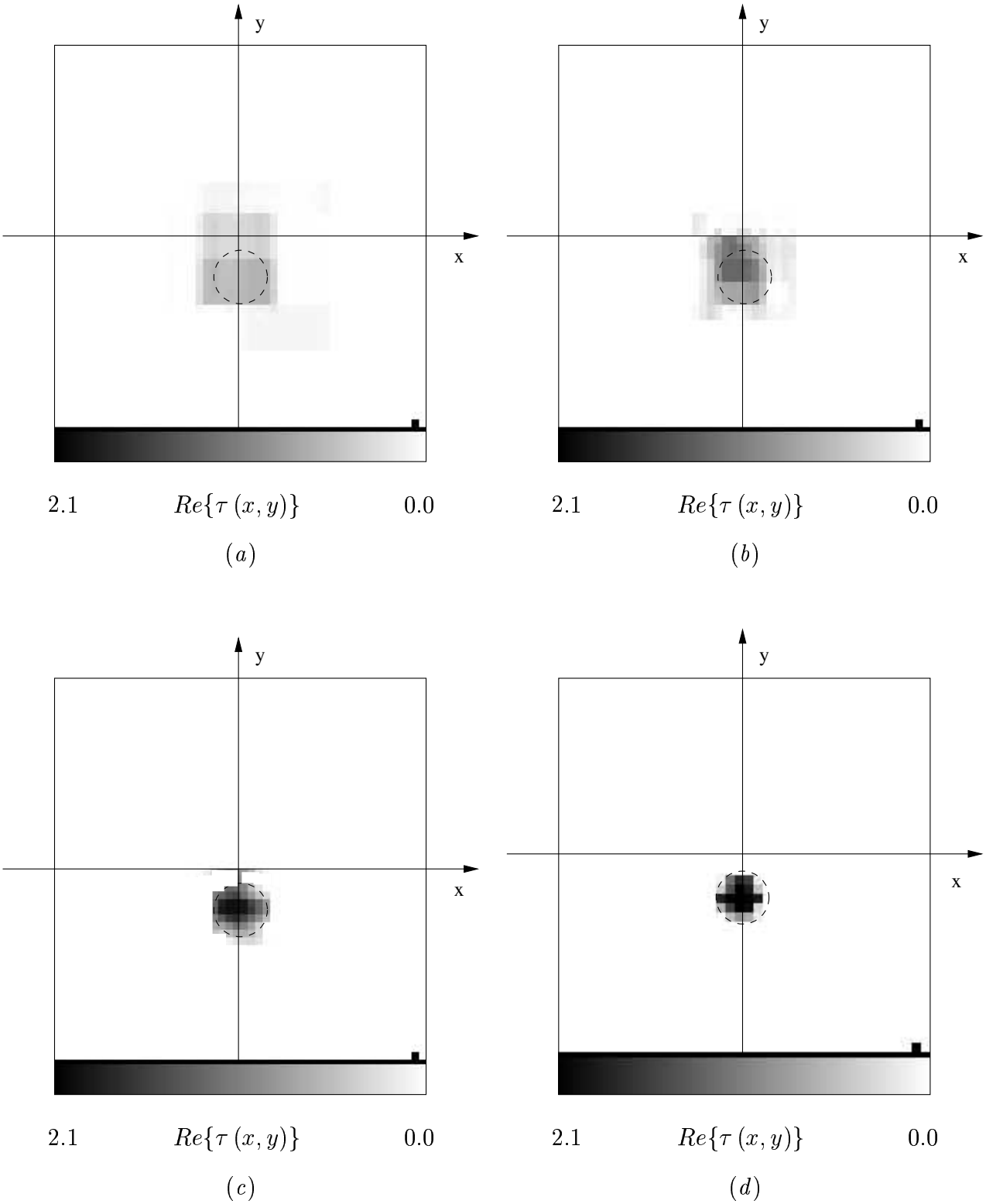

Fig. 17 - M. Donelli *et al.*, "A computational approach based on ..."

Reconstruction Procedure	ε_{tot}	ε_{int}	ε_{ext}	ρ	δ
PSO	2.49	3.91	1.52	6.0×10^{-3}	5.38
CG	10.21	18.39	9.71	6.4×10^{-3}	10.33
GA	3.58	7.29	3.03	9.7×10^{-3}	9.91

Tab. I - M. Donelli *et al.*, "A computational approach based on ..."

Step No.	ε_{tot}	ε_{int}	ε_{ext}	ρ	δ
1	3.93	4.10	1.55	1.1×10^{-3}	5.52
2	3.04	3.76	1.09	0.9×10^{-3}	5.05
3	1.01	1.14	0.45	1.8×10^{-4}	1.14

Tab. II - M. Donelli *et al.*, "A computational approach based on ..."

Reconstruction Strategy	ε_{tot}	ε_{int}	ε_{ext}	ρ	δ	S^{opt}	K^{opt}
$IMM-PSO$	0.49	2.21	5.0×10^{-3}	0.2×10^{-4}	1.22	3	6000
$IMM-CG$	0.95	4.21	1.9×10^{-1}	1.2×10^{-4}	2.08	3	4000
$IMM-GA$	0.60	3.99	3.5×10^{-2}	1.9×10^{-3}	1.99	3	6000

Tab. III - M. Donelli *et al.*, "A computational approach based on ..."

$SNR\ [dB]$	ε_{tot}	ε_{int}	ε_{ext}	ρ	δ	S^{opt}	K^{opt}
$Noiseless$	0.49	2.21	5.0×10^{-3}	0.2×10^{-4}	1.22	3	6000
20	2.45	4.21	9.1×10^{-2}	1.2×10^{-4}	3.58	2	4000
10	4.49	6.11	7.2×10^{-1}	1.1×10^{-3}	3.23	2	4000
5	8.25	15.23	1.5×10^{0}	2.1×10^{-1}	6.91	2	4000

Tab. IV - M. Donelli *et al.*, "A computational approach based on ..."

Reconstruction Strategy	ε_{tot}	ε_{int}	ε_{ext}	ρ	δ	S^{opt}	K^{opt}
$IMM-PSO$	4.42	6.82	1.66	4.1×10^{-2}	7.12	4	7570
$IMM-CG$	5.96	12.15	4.36	2.2×10^{-1}	10.65	3	6000

Tab. V - "**M. Donelli *et al.*,** "A computational approach based on ..."

Reconstruction Strategy	ε_{tot}	ε_{int}	ε_{ext}	ρ	δ	S^{opt}	K^{opt}
$IMM-PSO$	3.38	4.78	0.01	1.8×10^{-3}	4.82	3	6000
$IMM-GA$	5.01	5.07	0.92	3.0×10^{-2}	4.85	3	6000

Tab. VI - M. Donelli *et al.*, "A computational approach based on ..."

$Reconstruction\ Strategy$	$x_{c(S_{opt})}$	$y_{c(S_{opt})}$	$L_{(S_{opt})}$	$S_{(S_{opt})}$	$K_{(S_{opt})}$
$IMM-PSO$	-1.10	-30.2	31.06	3	5037
$IMM-CG$	-1.78	-26.15	30.72	2	4000

Tab. VII - M. Donelli *et al.*, "A computational approach based on ..."